

Learnable Activation Functions in Physics-Informed Neural Networks for Solving Partial Differential Equations

Afrah Farea^{a,*}, Mustafa Serdar Celebi^a

^aDepartment of Computational Science and Engineering, Istanbul Technical University, Istanbul 34469, Turkey

ARTICLE INFO

Keywords:

Partial differential equations
Physics Informed Neural networks
Multilayer Perceptrons
Kolmogorov-Arnold Networks
Learnable Activation Function

ABSTRACT

We investigate the use of learnable activation functions in Physics-Informed Neural Networks (PINNs) for solving Partial Differential Equations (PDEs). Specifically, we compare the efficacy of traditional Multilayer Perceptrons (MLPs) with fixed and learnable activations against Kolmogorov-Arnold Networks (KANs), which employ learnable basis functions. Physics-informed neural networks (PINNs) have emerged as an effective method for directly incorporating physical laws into the learning process, offering a data-efficient solution for both the forward and inverse problems associated with PDEs. However, challenges such as effective training and spectral bias, where low-frequency components are learned more effectively, often limit their applicability to problems characterized by rapid oscillations or sharp transitions. By employing different activation or basis functions on MLP and KAN, we assess their impact on convergence behavior and spectral bias mitigation, and the accurate approximation of PDEs. The findings offer insights into the design of neural network architectures that balance training efficiency, convergence speed, and test accuracy for PDE solvers. By evaluating the influence of activation or basis function choices, this work provides guidelines for developing more robust and accurate PINN models. The source code and pretrained models used in this study are made publicly available to facilitate reproducibility and future exploration.


1. Introduction

In recent years, neural networks, and particularly deep learning, have emerged as a promising tool for solving complex PDEs. These methods leverage universal approximation capabilities of networks to model nonlinear functions, offering significant advantages in high-dimensional, nonlinear PDE scenarios where traditional numerical methods are computationally expensive or complex [19, 10]. Neural networks offer several advantages: they are mesh-free, highly parallelizable, and can generate closed-form solutions, making them particularly useful for large-scale spatiotemporal problems [18, 22, 29, 3, 32, 65]. Additionally, they excel at handling noisy and incomplete data effectively, which further enhances their utility as alternatives to conventional solvers in real-world applications.

Among these neural network frameworks, Physics Informed Neural Networks (PINNs) [35] have gained significant attention due to their ability to incorporate physical laws directly into the learning process [35]. By embedding governing equations and boundary conditions as part of the loss function, PINNs offer a data-efficient approach to solving both forward and inverse PDE problems. This integration leads to highly accurate predictions even with limited data and allows for the discovery of unknown physical parameters [53]. While PINNs have proven successful across various domains, there are notable limitations, including spectral bias- a phenomenon where the network tends to learn low-frequency components more effectively than high-frequency ones [34, 9, 54]. In the context of solving PDEs, this means that solutions with sharp gradients or rapid oscillations (e.g., solutions to the wave propagation, convection-dominated flows, or problems involving turbulence) may converge slowly because the network struggles to capture high-frequency details early in training.

The recently introduced KANs [26] provide a new architecture rooted in the Kolmogorov-Arnold representation theorem. KANs employ learnable activation functions constructed from gridded basis functions, offering a more structured and interpretable alternative to traditional MLPs [33]. KAN's flexibility in handling different basis functions (e.g., splines or polynomials) and trainable scaling factors improves performance in various scientific tasks, including solving PDEs. Recent studies suggest that KANs exhibit reduced spectral bias, making them more effective in capturing high-frequency components, which is critical for accurately modeling multi-scale features [55, 20].

*Corresponding authors

 farea16@itu.edu.tr (A. Farea); mscelebi@itu.edu.tr (M.S. Celebi)

ORCID(s): 0000-0003-4412-5377 (A. Farea); 0000-0003-4566-0216 (M.S. Celebi)

Despite these advancements, there are areas for improvement in the effective application of KANs and PINNs for solving PDEs. For instance, the choice of appropriate hyperparameters such as **activation functions** or basis functions plays a critical role in the performance and optimization of both MLPs and KANs. Neural networks can be sensitive to activation function choices, with the spectral bias significantly impacting the convergence speed and accuracy of the solution [48]. Further exploration of various activation functions in the context of KANs and MLPs for different PDE problems can reveal crucial insights into how these architectural choices influence generalization and efficiency [37].

Spectral bias remains a challenge for both MLPs and KANs, as networks tend to prioritize learning low-frequency features over high-frequency ones. This issue becomes particularly problematic for PDEs with sharp transitions or multi-scale features, where capturing both high and low-frequency components is essential [61, 31]. Traditional numerical methods such as Multigrid Method (MG) [50, 8], address this issue by leveraging hierarchical grids to handle different frequency components in such a way that the iterative solvers used in MG, e.g., Jacobi or Gauss-Seidel, smooth out high-frequency components, while low-frequency errors are corrected on coarser grids. Similarly, neural networks, especially KANs with adaptive grid size, may offer a more balanced approach for approximating multi-scale PDEs.

A detailed comparison of these methods could provide further guidance for improving neural PDE solvers [42, 55]. This work attempts to address the above challenges and offers the following contributions:

1. **Exploration of learnable activations:** We perform an extensive comparison between KANs and traditional MLP-based PINNs, including MLPs with both fixed and learnable activation functions. Our results highlight the strengths and weaknesses of each approach, especially in terms of training convergence rates, testing error, and the networks' ability to capture high-frequency components.
2. **Study of Convergence and spectral bias behaviour:** We examine how KANs and MLPs with diverse basis functions or activation mechanisms converge to solutions and address spectral bias, particularly in their ability to capture high-frequency components in multi-scale PDEs. Using the maximum eigenvalue of the loss Hessian, we analyze each model's sensitivity and stability, providing insights into their convergence dynamics and capacity to approximate complex, high-frequency patterns accurately.
3. **Application to diverse PDEs:** We explore the applicability of MLPs and KANs across a wide range of PDEs, including Helmholtz [28, 25, 13, 52], Wave [5, 40], Klein-Gordon [17, 57], Convection-diffusion [38, 4], and Cavity [43, 16] problems as they serve as benchmarks [47, 62] for evaluating PINNs' effectiveness. By examining different activation and basis functions, e.g., Tanh, parameterized Tanh, B-splines, Gaussian Radial Basis Functions (GRBFs), Fourier, Chebyshev, and Jacobi polynomials, we assess how these architectural choices affect the network's capacity to capture critical features of PDE solutions.

The findings of this study provide valuable insights into designing neural network architectures for PDE solvers that balance training efficiency, convergence speed, and test accuracy. By analyzing the effects of different activation functions, basis functions, and network architectures, this work offers insights into better design choices for developing more robust and accurate PINNs.

The source code and pre-trained models used in this study are publicly available at https://github.com/afrah/pinn_learnable_activation.git, allowing for reproducibility and further exploration.

2. Related Work

Using adaptive methods to enhance the performance of PINNs was deeply invested in literature [17, 27, 6, 59, 24, 49, 67, 1, 66] where different adaptive methods based on different criteria are proposed to better capture problem dynamics and enhance training efficiency. Adaptive activation functions, in particular, play a crucial role by increasing the network's expressivity and minimizing the need for manual hyperparameter tuning. These functions dynamically adjust to the characteristics of the specific task. Although this adaptability adds complexity to the training process, it enables PINNs to capture complex solution landscapes more effectively, enhancing both accuracy and convergence.

The authors in [2] classify learnable activation functions into two categories. The first category is parameterized standard activation functions, in which specific parameters are learned during training. For example, the original Swish activation proposed in [36] has the form $x \cdot \sigma(\beta x)$ where β is a constant or learnable parameter. The second category consists of functions based on ensemble methods, where multiple candidate activation functions or models

are combined to create more flexible and adaptable activation functions such that $f(x) = \sum_{i=1}^h \alpha_i g_i(x)$ where $g_i(x)$ is a linear mapping, and α_i are learnable weights. Sütfield et al.[45] proposed Adaptive Blending Units (ABUs) that combine a set of basic activation functions through learnable blending weights, allowing the neural network to learn an optimal activation shape for each layer during training. Wang et al., in [51] follow a similar approach with g_i as a standard activation function and experimentally show that this method outperforms the fixed actuation function. However, the success of this method depends on the diversity and suitability of the candidate activation functions, and the complexity increases with an increasing number of candidate functions. Jagtap et al.[17] study the effect of adaptive action function on PINN when solving Helmholtz and Klein-Gordon equations. The study demonstrates that using adaptive activation functions significantly enhances the training process, especially in capturing complex frequencies in the solutions.

In the original work, Liu et al. [26] demonstrate that the proposed KAN model with B-spline basis function can accurately solve the Poisson equation, outperforming MLPs in accuracy and parameter efficiency. The network structure in KANs learns a combination of simpler functions akin to the ensemble methods. More specifically, the base learners ($g_i(x)$) and the weighted sum α_i in the ensemble methods correspond to the univariate ϕ_{ij} and the outer functions ψ_i in KAN, respectively. The key difference between KAN and ensemble functions like Adaptive Blending Units (ABUs) [45] lies in their approach to function representation: KAN focuses on building a universal approximation by decomposing a multivariate function into a sum of univariate functions, leveraging the Kolmogorov-Arnold representation theorem. However, the ensemble functions blend multiple activation functions, optimizing their combinations through learned weights to adaptively change the activation shape during training.

Zang et al. [64] examine various function types, including regular, non-differentiable, jump discontinuities, singularities, and noisy functions, to assess how well KAN and MLP perform under different conditions. The results show that KAN performs better on regular functions, but MLP generally outperforms KAN on functions with irregularities like discontinuities and singularities. The results also show that both models struggle with noisy data.

Hong et al. [15] show that the spectral bias in the neural network depends on the activation function and study how networks with ReLU activation exhibit a preference for learning low-frequency components faster than high-frequency ones. By drawing parallels to finite element methods, they provide both theoretical insights and empirical evidence demonstrating that this spectral bias can be alleviated by using the "Hat" function—a piecewise linear spline that generalizes the ReLU activation function. Their findings reveal that networks with this Hat function exhibit a more balanced learning behavior across frequency spectra. Extending this concept further, KANs with learnable, higher-order B-splines as activation functions offer smoothness, flexibility, and adaptive control over learning frequency content. Recent work by Wang et al. [55] has shown that KANs significantly reduce spectral bias compared to MLPs, enhancing their ability to represent complex functions. Shukla et al. [42] introduce Physics-Informed KANs (PIKANs) and DeepOKANs. They also show that KAN with the Chebyshev basis function shows more stability with lower learning rate values and recursive formulation. [39] [39] introduces an open-source, JAX-based implementation of KANs and adaptive grid-dependent training techniques to address issues like abrupt loss peaks during grid extension, thereby improving convergence and stability. Their findings highlight that KAN-based architectures can achieve higher accuracy with fewer parameters, making them a viable and efficient alternative to MLP-based PINNs in specific PDE applications. Wang et al. [56] demonstrate that KAN-based models significantly outperform MLP-based models in solving a set of PDE equations, highlighting their effectiveness compared to MLP-based models.

3. Problem Formulation and Neural Network Methods

The general differential equation has the form,

$$\begin{aligned} D[u(\mathbf{x}); \alpha] &= f(\mathbf{x}), \quad \mathbf{x} \in \Omega, \\ B[u(\mathbf{x})] &= g_k(\mathbf{x}), \quad \mathbf{x} \in \Gamma_k \subset \partial\Omega, \quad k = 1, 2, \dots, n_b \end{aligned} \tag{1}$$

where D is the differential operator, B is a set of boundary operators, $f(\mathbf{x})$ is the forcing function, $g_k(\mathbf{x})$ is a set of boundary functions, α is a set of parameters used in the differential equation and $u(\mathbf{x})$ is the solution of the differential equation given input \mathbf{x} in the solution domain Ω with boundary $\partial\Omega$.

This work considers five PDEs as use cases discussed in section 4. For completeness, we briefly review the concepts of MLP, KAN, and the basic algorithm of the KAN model with a general basis function in the following subsections.

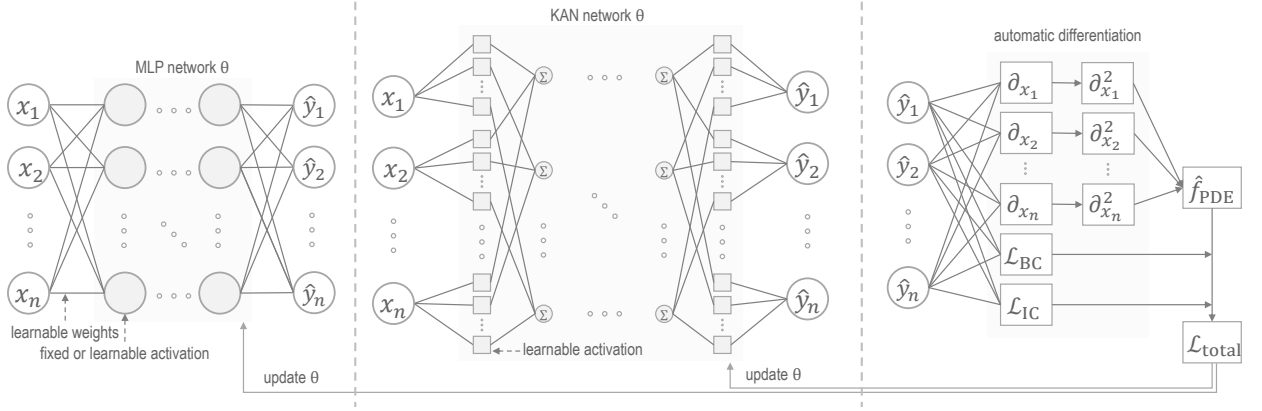


Figure 1: This diagram presents a high-level comparison between the MLP and KAN architectures within the PINN framework. The MLP network uses learnable weights with nonlinear activation functions during training. In contrast, KAN incorporates learnable activation functions. The MLP and KAN networks pass the outputs to the Physics module, which uses automatic differentiation (AD) to calculate physics loss.

3.1. Multilayer Perceptron (MLP) Approximation

At the core of neural network models lies the Multilayer Perceptron (MLP), valued for its ability to capture complex, non-linear relationships within data. The effectiveness of MLPs is theoretically grounded in the universal approximation theorem [11], which asserts that a feedforward network with a single hidden layer containing $k > N(\epsilon)$ neurons can approximate any continuous function on a compact subset of \mathbb{R}^N to within a specified error ϵ . In its simplest form, an MLP consists of a finite set of inputs x_i , each associated with a learnable weight w_{ij} , representing the connection strength of neuron j in layer i , and a bias term that adjusts the neuron's output. The output of a perceptron can be represented as:

$$f_i = \phi \left(\sum_{j=0}^{n+1} w_{ij} x_j \right), \quad x_0 = 1 \quad (2)$$

where w_{ij} includes the bias term for neuron i in layer j , and $\phi(\cdot)$ denotes the activation function. The activation function is crucial; it must be nonlinear and differentiable to enable the network to capture complex patterns and compute gradients efficiently during backpropagation. Ideally, the activation function is smooth enough to ensure stable gradient behavior during optimization and unbounded enough to mitigate vanishing and exploding gradients. In the context of PDEs, the activation function should have well-defined, higher-order, smooth, continuous derivatives that facilitate accurate backpropagation and allow the network to adhere closely to the PDE's requirements.

Fig. 1(left) depicts the structure of a typical MLP model with learnable weights and activation functions used to map inputs to outputs. The activation functions in MLP can be either set to a specific function (like ReLU or Tanh) or have parameters that can be adjusted during training.

3.2. Kolmogorov-Arnold Approximation

According to Kolmogorov-Arnold representation theorem [21], any multivariate continuous function f of n variables on a bounded domain can be represented by a superposition of a finite number of continuous functions with a single variable and the summation operation. More formally, for any continuous function $f : \mathbb{R}^n \rightarrow \mathbb{R}$, there exist continuous functions ϕ_i and ψ such that

$$f(x_1, x_2, \dots, x_n) = \sum_{i=1}^{2n+1} \psi_i \left(\sum_{j=1}^n \phi_{ij}(x_j) \right), \quad (3)$$

where x_1, x_2, \dots, x_n are the input variables, $\psi_i : \mathbb{R} \rightarrow \mathbb{R}$ and $\phi_{ij} : [0, 1] \rightarrow \mathbb{R}$ are continuous univariate functions, $1 \leq i \leq 2n + 1$ and $1 \leq j \leq n$. In other words, KANs do not use activation functions in the same way used in MLPs. Instead, they use learnable univariate activation functions ϕ_{ij} , typically parameterized as B-splines [12].

The original work, Liu et al. [26] uses SiLU as the base activation function to capture the non-linear relationships that could not be captured by the B-spline network as follows:

$$\phi(x) = \lambda_0 \text{silu}(x) + \lambda_1 \text{spline}(x) = \lambda_0 \text{silu}(x) + \lambda_1 \sum_{i=1}^{d+k-1} c_i B_i(x)$$

where d is the spline order, k is the grid size, λ_0 , λ_1 and c_i are trainable parameters, $B_i(x)$ is the B-spline function. The ranges of the grid points of the B-splines are updated on the fly based on the range of the previous layer's output.

Although B-splines are commonly used due to their flexibility and smoothness properties, alternative functional forms such as Chebyshev polynomials [44], Radial Basis Functions (RBF)[23, 46], Fourier [60], and wavelet [7, 41] or any other basis function can also be used for ϕ . These alternatives may offer specialized basis functions based on the nature and application of the problem, making KAN a general framework for function approximation. More generally, Algorithm 1 shows the steps for parametrization of the activation function within the KAN formulation. The main idea is to map the inputs of each neural network layer to a higher-dimensional space using a suitable basis function, multiply the result by learnable parameters, and optimize iteratively.

Fig. 1(middle) illustrates the structure of KAN with learnable activation functions. The basis activation functions are parametrized and updated like standard weights through backpropagation and gradient descent.

Algorithm 1 A KAN model with a general basis function.

Require: x : input data of shape $[\text{batch_size}, l_0]$, network : $[l_0, l_1, \dots, l_n]$, d : degree of basis function

Ensure: y : output of the model for input x

```

1: Initialize an empty list layers
2: for each layer  $(l_i, l_{i+1})$  in  $\text{network}$  do
3:   Create a new KAN layer  $L_i$  with input dimension  $l_i$ , output dimension  $l_{i+1}$ 
4:   Initialize learnable coefficients  $\text{coeffs}_{ij}$  for each layer  $L_i$ 
5:   Append layer  $L_i$  to layers
6: end for
7: Forward Pass:
8: If required, normalize  $x$  to the domain of the basis function
9: for each layer  $L_i$  in layers do
10:  Compute  $B(x) \leftarrow \text{basis\_function}(x, d)$ 
11:  Compute  $y \leftarrow \sum_{j=0}^d \text{coeffs}_{ij} \cdot B_j(x)$ 
12: end for
13: return  $y$ 
14: Function:  $\text{basis\_function}(x, d)$ 
15:   Generate basis function  $B(x)$  from input  $x$  and degree  $d$ 
16:   return  $B(x)$ 

```

Table 1 presents several well-known basis functions that we considered for solving PDEs due to their unique characteristics and mathematical properties. These basis functions are smooth with varying degrees of differentiability, depending on factors such as polynomial degrees or specific function coefficients. For example, while cubic or high-degree B-splines are differentiable and smooth, the Fourier basis functions have differentiability tied directly to their coefficients, making them versatile for periodic functions. These characteristics make these basis functions promising candidates for learnable activation functions within the MLP architecture, providing increased expressiveness at the cost of added computational complexity. However, leveraging such basis functions as learnable activations can also introduce challenges, particularly in training stability. The increased complexity may lead to issues such as vanishing or exploding gradients during backpropagation, especially in deep networks or when higher-degree polynomials are used. Furthermore, numerical stability may become a concern, as many of these functions are sensitive to inputs outside their well-defined intervals, potentially leading to significant calculation errors. Despite these challenges, the

Table 1

KAN basis functions considered in the study and Tanh activation function. O : the number of parameters in terms of asymptotic notation, n : the number of units per hidden layer, L : the number of hidden layers, k : the grid size, and d : the degree of the polynomial basis function.

Basis Function	Equation	Local Support	Global Support	Node Requirement	Numerical stability	Smoothness	Boundedness	Number of Parameters	Suitability
Radial Basis Function	$e^{-\frac{\ x-c\ ^2}{\sigma^2}}$	✓	✗	✓	✓	✓	[0, 1]	$\mathcal{O}(n^2 \cdot L \cdot k)$	Interpolation, Spatial Modelling
B-spline	$B_{i,n}(x) = \frac{x-t_i}{t_{i+n}-t_i} B_{i,n-1}(x) + \frac{t_{i+n+1}-x}{t_{i+n+1}-t_{i+1}} B_{i+1,n-1}(x)$	✓	✗	✓	✓	✓	Implementation dependent	$\mathcal{O}(n^2 \cdot L \cdot (k + d - 1))$	Piecewise Polynomial Approximation, Curve Fitting
Chebyshev	$T_d(x) = 2xT_{d-1}(x) + T_{d-2}(x)$	✗	✓	✓	✓	✓	[-1, 1]	$\mathcal{O}(n^2 \cdot L \cdot (d+1))$	Spectral Methods, Polynomial Approximation
Jacobi	$P_d^{(\alpha,\beta)}(x) = \frac{(-1)^d}{2^d d!} (1-x)^{-\alpha} (1+x)^{-\beta} \mathcal{D}^d [(1-x)^{\alpha+d} (1+x)^{\beta+d}]$	✗	✓	✓	✓	✓	[-1, 1]	$\mathcal{O}(n^2 \cdot L \cdot (d+1))$	Weighted Polynomial Approximation
Fourier	$\sum_k a_k \cos(kx) + b_k \sin(kx)$	✗	✓	✗	✓	✓	Coefficients a_k and b_k dependent	$\mathcal{O}(n^2 \cdot L \cdot k)$	Periodic Functions, Signal Processing
Tanh	$\tanh(x) = \frac{e^x - e^{-x}}{e^x + e^{-x}}$	✗	✓	✗	✓	✓	[-1, 1]	$\mathcal{O}(n^2 \cdot L)$	Smooth, global pattern

expressive power and flexibility of these basis functions make them valuable tools for modeling complex physical phenomena in PDE-based applications.

The Tanh activation function is well-known to suffer from vanishing and exploding gradients when inputs deviate significantly from zero, as its gradient diminishes toward zero when $\tanh(x) \rightarrow \pm 1$. This behavior can hinder the learning process in deep networks, especially in cases requiring large-weight updates. Likewise, polynomial basis functions (such as Chebyshev, Legendre, Hermite, Jacobi, and Laguerre polynomials) can lead to gradient issues. Near-zero polynomial values often cause vanishing gradients, while higher-degree polynomials grow rapidly for large x , resulting in excessively large derivatives outside the interval $[-1, 1]$ and causing exploding gradients during backpropagation. This sensitivity to input scale and polynomial degree can destabilize training.

Radial Basis Functions (RBFs) are also prone to vanishing gradients when the input is far from the center c_i , especially if the scaling factor σ is not optimal, as the gradient approaches zero in these regions. While higher-degree splines generally offer stability, improper scaling or poor placement of knots can induce both vanishing and exploding gradients. In addition, Fourier basis functions can cause gradient explosions when high frequencies dominate, leading to rapid oscillations. This oscillatory behavior increases gradient magnitude significantly, which can make training unstable, particularly in the presence of high-frequency terms.

These challenges underscore the importance of carefully selecting and scaling activation and basis functions to maintain stable gradients and prevent issues during backpropagation, especially in applications involving deep or physics-informed neural networks.

3.3. Physics Informed Neural Networks (PINN)

Before PINNs [35], neural networks used in solving PDEs primarily relied on large simulation or experimental data datasets to learn patterns and make predictions, which may cause overfitting or lack of generalization. PINNs integrate physical laws directly into the neural network's learning process by embedding the governing equations (such as the Navier-Stokes equations) into the loss function. The idea is to recover the unique solution of the PDE by penalizing the boundary and initial conditions as data-driven supervised learning and choosing finitely many representative points from the interior that satisfy the differential equation. For instance, to approximate the solution of the PDE equation 1, we train the PINN model by minimizing the loss function of the form:

$$\begin{aligned} \mathcal{L}(\theta) &= \underset{\theta}{\operatorname{argmin}} \sum_{k=1}^n \lambda_k \mathcal{L}_k(\theta) \\ &= \underset{\theta}{\operatorname{argmin}} \left(\lambda_1 \mathcal{L}(\mathcal{D}[u(\mathbf{x}); \alpha] - f(\mathbf{x})) + \sum_{k=2}^{n_b} \lambda_k \mathcal{L}(\mathcal{B}[u(\mathbf{x})] - g_k(\mathbf{x})) \right) \end{aligned} \quad (4)$$

where n is the number of loss terms, λ_k is the weighting coefficient of the respective loss term. No prior knowledge of the actual solution $u(\mathbf{x})$ is required, as minimizing equation (4) yields the desired solution. Notably, equation (4) reduces the multi-objective constraints of the PDE (1) into a single constraint. An important observation here is that this loss function may include terms with different physical scales, particularly when high-order derivatives are present in the physics loss, potentially impacting the quality and stability of training. Such an aggregation makes the loss landscape of PINNs highly nonconvex, often containing numerous local minima and saddle points. This nonconvexity poses significant challenges for optimization, especially when coupled with the vanishing gradient problem commonly associated with MLPs. In PINNs, this problem is further exacerbated, as the physical constraints embedded within the loss function can lead to even smaller gradients, making effective learning more challenging—particularly in deeper architectures. This effect complicates the training process, hindering the network’s ability to capture complex solution features and making it especially difficult to learn high-order derivatives and multi-scale behaviors essential in many physical systems.

Fig. 1(right) illustrates the structure of PINN, where the outputs of the network (either MLP or KAN) are used to solve PDEs by enforcing physics-based constraints through automatic differentiation. The network must also satisfy the PDE’s boundary conditions (and, for time-dependent PDEs, initial conditions). These terms are then combined into a total loss, \mathcal{L}_{loss} , which is minimized during training to ensure the network learns the differential equation and associated conditions properly.

4. Use Cases

This section outlines the various selected 1- and 2-D PDE equations, boundary condition settings, and loss functions used for evaluation.

4.1. 1D Wave Equation

The wave equation is a second-order hyperbolic partial differential equation that models the propagation of waves, such as sound or vibrations, through a medium. We consider the time-dependent 1D wave equation of the form,

$$\begin{aligned}
u_{tt}(t, x) - c^2 u_{xx}(t, x) &= 0 & (t, x) &\in \Omega \\
u(t, x_0) &= f_1(t, x) & (t, x) &\text{ on } \Gamma_0 \\
u(t, x_1) &= f_2(t, x) & (t, x) &\text{ on } \Gamma_1 \\
u(0, x) &= g(t, x) & (t, x) &\in \Omega \\
u_t(0, x) &= h(t, x) & (t, x) &\in \partial\Omega
\end{aligned} \tag{5}$$

where c is the wave speed. We set $c = 2$, $a = 0.5$, $f_1 = f_2 = 0$ and exact solution of the form, $u(t, x) = \sin(\pi x)\cos(c\pi t) + 0.5\sin(2c\pi x)\cos(4c\pi t)$ on the domain $(t, x) \in [0, 1] \times [0, 1]$. The equation becomes,

$$\begin{aligned}
u_{tt}(t, x) - 4u_{xx}(t, x) &= 0 & (t, x) &\in \Omega = [0, 1] \times [0, 1] \\
u(t, 0) = u(t, 1) &= 0 \\
u(0, x) &= \sin(\pi x) + 0.5\sin(4\pi x) & x &\in [0, 1] \\
u_t(0, x) &= 0
\end{aligned} \tag{6}$$

The loss function for solving the problem with PINN is:

$$\begin{aligned}
\mathcal{L}(\theta) &= \min_{\theta} (\lambda_1 \|\mathcal{L}_{phy}(\theta)\|_{\Omega} + \lambda_2 \|\mathcal{L}_{bc}(\theta)\|_{\Gamma_1} + \lambda_3 \|\mathcal{L}_{ic}(\theta)\|_{\Gamma_0}) \\
&= \min_{\theta} (\lambda_1 \mathcal{L} \|u_{\theta_{tt}}(t, x) - 4u_{\theta_{xx}}(t, x)\|_{\Omega} + \lambda_2 \mathcal{L} \|u(t, 0) + u(t, 1) + u(0, x)\|_{\Gamma_1} + \lambda_3 \mathcal{L} \|u_{\theta_t}(0, x)\|_{\partial\Omega})
\end{aligned} \tag{7}$$

We set 1.0, 100.0, 100.0 for $\lambda_1, \lambda_2, \lambda_3$ respectively. The difficulty of this problem lies in the presence of high-frequency components in the solution and the nonlinearity introduced by the interaction between time and space, which makes it more challenging for neural networks to capture without sufficient expressivity.

4.2. Helmholtz Equation

The Helmholtz equation is a time-independent form of the wave equation arising in many physical problems like vibrating membranes, acoustics, and electromagnetism. We consider a 2D Helmholtz equation of the form,

$$\begin{aligned} \Delta u(x, y) + k^2 u(x, y) &= q(x, y) & (x, y) \in \Omega \\ u(x, y) &= h(x, y) & (x, y) \in \Gamma_0 \end{aligned} \quad (8)$$

where Δ is the Laplacian operator ($\Delta u = u_{xx} + u_{yy}$), $q(x, y)$ is the forcing term, and k is the wavenumber. For simplicity, we assume Dirichlet boundary conditions ($h(x, y)$) equal to an exact solution of the form, $u(x, y) = \sin(a_1 \pi x) \sin(a_2 \pi y)$ corresponding to the source term $q(x, y) = u(x, y)[k^2 - (a_1 \pi)^2 - (a_2 \pi)^2]$ with $k = 1, a_1 = 1, a_2 = 4$. The final form of the equation with the boundary and initial conditions is,

$$\begin{aligned} \Delta u(x, y) + u(x, y)[(a_1 \pi)^2 + (a_2 \pi)^2] &= 0 & (x, y) \in \Omega = [-1, 1] \times [-1, 1] \\ u(x, y) &= 0 & (x, y) \in \Gamma_0 \end{aligned} \quad (9)$$

The loss function for solving the problem with PINN is:

$$\begin{aligned} \mathcal{L}(\theta) &= \min_{\theta} (\lambda_1 \|\mathcal{L}_{phy}(\theta)\|_{\Omega} + \lambda_2 \|\mathcal{L}_{bc}(\theta)\|_{\Gamma_0}) \\ &= \min_{\theta} (\lambda_1 \mathcal{L} \|u_{\theta_{xx}}(x, y) + u_{\theta_{yy}}(x, y) + \alpha u_{\theta}(x, y)\|_{\Omega} + \lambda_2 \mathcal{L} \|u_{\theta}(x, y) - u(x, y)\|_{\Gamma_0}) \end{aligned} \quad (10)$$

We set 1.0, 10.0 for λ_1, λ_2 respectively.

4.3. Klein-Gordon Equation

Klein-Gordon equation is a second-order hyperbolic partial differential equation that appears in various fields such as quantum field theory, general relativity, and nonlinear optics. We consider 1D nonlinear Klein-Gordon equation of the form,

$$\begin{aligned} u_{tt} - \alpha u_{xx} + \beta u + \gamma u^k &= 0 & (t, x) \in \Omega \\ u(t, x) &= g_1(t, x) & (t, x) \\ u_t(t, x) &= g_2(t, x) & (t, x) \\ u(0, x) &= h(t, x) & (t, x) \in \partial\Omega \times [0, T] \end{aligned} \quad (11)$$

where α, β, γ and k are known constants. We set 1, 0, 1, 3 for α, β, γ and k respectively. We use the exact solution of the form, $u(t, x) = x \cos(5\pi t) + (tx)^3$. The final form of the equation with the boundary and initial conditions is,

$$\begin{aligned} u_{tt}(t, x) - \alpha u_{xx}(t, x) + \beta u(t, x) + u^3(t, x) &= 0 & (t, x) \in \Omega = [0, 1] \times [0, 1] \\ u(t, 0) &= 0 & (t, x) \\ u(t, 1) &= \cos(5\pi t) + (t)^3 & (t, x) \\ u(0, x) &= x & (0, x) \\ u_t(0, x) &= 0 & (0, x) \end{aligned} \quad (12)$$

The loss function for solving the problem with PINN is:

$$\begin{aligned} \mathcal{L}(\theta) &= \min_{\theta} (\lambda_1 \|\mathcal{L}_{phy}(\theta)\|_{\Omega} + \lambda_2 \|\mathcal{L}_{bc}(\theta)\|_{\Gamma_1} + \lambda_3 \|\mathcal{L}_{ic}(\theta)\|_{\Gamma_0}) \\ &= \min_{\theta} (\lambda_1 \mathcal{L} \|u_{\theta_{tt}}(t, x) - u_{\theta_{xx}}(t, x) + u^3(t, x)\|_{\Omega} + \lambda_2 \mathcal{L} \|u(t, 0) + u(t, 1) + u(0, x)\|_{\Gamma_1} + \lambda_3 \mathcal{L} \|u_{\theta_t}(0, x)\|_{\partial\Omega}) \end{aligned} \quad (13)$$

We set 1.0, 50.0, 50.0 for $\lambda_1, \lambda_2, \lambda_3$ respectively.

4.4. Convection-diffusion Equation

Convection-diffusion Equation is a second-order partial differential equation that models the transport of a substance (or a quantity like heat) in a medium, considering both convection (movement due to flow) and diffusion (spreading out due to concentration gradients). We consider the viscous 2D convection-diffusion equation of the form,

$$\begin{aligned}
 u_t + c_1 u_x + c_2 u_y - D \Delta u(x, y) &= 0 & (t, x, y) \in \Omega \\
 u(t, \mathbf{x}) &= g_0(t, \mathbf{x}) & (t, \mathbf{x}) \in \Gamma_0 \\
 u(t, \mathbf{x}) &= g_1(t, \mathbf{x}) & (t, \mathbf{x}) \in \Gamma_1 \\
 u(0, \mathbf{x}) &= h(0, \mathbf{x}) & \mathbf{x} \in \partial\Omega \times [0, T]
 \end{aligned} \tag{14}$$

where c_1 and c_2 are the convection velocities in the x and y directions respectively, D is the diffusion coefficient, and Δ is the Laplacian operator. We use an exact solution of the form $u(t, x, y) = \exp(-100((x-0.5)^2 + (y-0.5)^2)) \exp(-t)$ which describes a Gaussian pulse centered at $(x, y) = (0.5, 0.5)$ that decays over time. The corresponding to the initial condition is $h(0, x, y) = \exp(-100((x-0.5)^2 + (y-0.5)^2))$. For this particular problem, later timesteps are important because the system has evolved, and the solution becomes more diffuse and less concentrated. As a result, it becomes harder for models to accurately capture the subtle diffusion and dissipation effects.

We set 1.0, 1.0, and 0.01 for c_1 , c_2 , and D , respectively. The final form of the equation with the boundary and initial conditions is,

$$\begin{aligned}
 u_t(t, x, y) + c_1 u_x(t, x, y) + c_2 u_y(t, x, y) - D (u_{xx}(t, x, y) + u_{yy}(t, x, y)) &= 0 & (t, x, y) \in \Omega = [0, 1] \times [0, 1] \times [0, 1] \\
 u(t, x, y) &= g(t, x, y) & (t, x, y) \in \Omega \\
 u(0, x, y) &= h(x, y) & (x, y) \in \partial\Omega \times [0, T]
 \end{aligned} \tag{15}$$

The loss function for solving the problem with PINN is:

$$\begin{aligned}
 \mathcal{L}(\theta) &= \min_{\theta} (\lambda_1 \|\mathcal{L}_{\text{phy}}(\theta)\|_{\Omega} + \lambda_2 \|\mathcal{L}_{\text{bc}}(\theta)\|_{\Gamma_1} + \lambda_3 \|\mathcal{L}_{\text{ic}}(\theta)\|_{\Gamma_0}) \\
 &= \min_{\theta} (\lambda_1 \|u_{\theta_t}(t, x, y) + v_x u_{\theta_x}(t, x, y) + v_y u_{\theta_y}(t, x, y) - D(u_{\theta_{xx}}(t, x, y) + u_{\theta_{yy}}(t, x, y))\|_{\Omega} \\
 &\quad + \lambda_2 \|u(t, x, y) - g_1(t, x, y)\|_{\Gamma_1} + \lambda_3 \|u_{\theta}(0, x, y) - h(x, y)\|_{\Omega_0})
 \end{aligned} \tag{16}$$

We set 1.0, 10.0, 10.0 for $\lambda_1, \lambda_2, \lambda_3$ respectively.

4.5. Time-dependent 2D Cavity Problem

This problem is a widely recognized Computational Fluid Dynamics (CFD) benchmark. It involves simulating the movement of cavity walls to drive fluid flow within the cavity. In this case study, the upper boundary moves at a constant velocity, creating a shear-driven flow inside the cavity, while the other boundaries remain stationary. The problem is governed by the unsteady, incompressible Navier-Stokes equations as follows:

$$\begin{aligned}
 \rho \left(\frac{\partial \mathbf{u}}{\partial t} + \mathbf{u} \cdot \nabla \mathbf{u} \right) &= -\nabla p + \mu \nabla^2 \mathbf{u} & \text{in } \Omega \in [0, 1] \\
 \nabla \cdot \mathbf{u} &= 0 & \text{in } \Omega \\
 \mathbf{u}(0, x) &= 0 & \text{in } \Omega \\
 \mathbf{u}(t, x_0) &= 0 & \text{on } \Gamma_1 \\
 \mathbf{u}(t, x_l) &= 1 & \text{on } \Gamma_0
 \end{aligned} \tag{17}$$

The computation domain Ω is a two-dimensional square cavity $\Omega = (0, 1) \times (0, 1)$. Uniform discretization is used with grid $(N_x, N_y) = (100, 100)$ and 10 seconds total simulation time with 0.01s time interval. Γ_1 is the top Dirichlet boundary condition of the cavity with velocity tangent to this side, Γ_0 denotes the other three stationary sides, $\rho = 1056$,

and $\mu = 1/Re = 0.01$ where Re the Reynolds number of the flow and ρ is the fluid density. We used the finite volume method to compare with the neural network approximation results.

The loss function for solving the Cavity problem is as follows:

$$\mathcal{L}(\theta) = \lambda_1 \|\mathcal{L}_{phy}\|_{\Omega} + \lambda_2 (\|\mathcal{L}_{up}\|_{\Gamma_1} + \|\mathcal{L}_{bc_1}\|_{\Gamma_0}) + \lambda_3 \|\mathcal{L}_{u0}\|_{\Omega} \quad (18)$$

where $\mathcal{L}_{phy}(\theta) = \mathcal{L}_{r_u} + \mathcal{L}_{r_v} + \mathcal{L}_{r_c}$. We select 0.1, 2.0, 4.0 for the $\lambda_1, \lambda_2, \lambda_3$ respectively such that,

$$\begin{aligned} \mathcal{L}_{r_u}(\theta) &= \text{MSE} \left[(\hat{u}_t + \hat{u}\hat{u}_x + \hat{v}\hat{u}_y) + \frac{1.0}{\rho} \hat{p}_x - \mu(\hat{u}_{xx} + \hat{u}_{yy}) \right] \\ \mathcal{L}_{r_v}(\theta) &= \text{MSE} \left[(\hat{v}_t + (\hat{u}\hat{v}_x + \hat{v}\hat{v}_y + \frac{1.0}{\rho} \hat{p}_y - \mu(\hat{v}_{xx} + \hat{v}_{yy})) \right] \\ \mathcal{L}_{r_c}(\theta) &= \text{MSE} [(\hat{u}_x + \hat{v}_y)] \end{aligned}$$

With the boundary and initial conditions:

$$\begin{aligned} \mathcal{L}_{up} &= \text{MSE} [(1.0 - \hat{u} + (\hat{v}))] \\ \mathcal{L}_{bc_1} &= \mathcal{L}_{\text{bottom, right, left}} = \text{MSE} [(\hat{u} + \hat{v})] \\ \mathcal{L}_{u_0} &= \text{MSE} [\hat{u}] + (\hat{v}) + (\hat{p}) \end{aligned}$$

5. Computational Experiments

5.1. Experiment Setup

Table 2 shows two groups of neural network architectures (see Fig. 1) and their settings used in this study: A1 and A2. The A1 architectures are designed with fewer neurons or parameters, while A2 architectures include more neurons, thereby increasing total number of parameters and model complexity and enhancing expressivity for function approximation.

We employed identical training settings for shared parameters to ensure a fair comparison between PINN with MLP and KAN models. All models were trained using the PyTorch Adam optimizer with hyperparameters $\beta_1 = 0.9$, $\beta_2 = 0.999$, $\epsilon = 10^{-8}$ and learning rate of $\eta = 0.001$ and a weight decay of $10e-6$. We applied Xavier initialization to initialize the weights of all models and minibatch training with batch size 128, sampled randomly for 60,000 iterations. We used float32 integer representation and Python `time.time()` for time measurement.

In the MLP models, we tested two variants with different activation functions: standard Tanh and parametric-Tanh. The standard model used Tanh as its activation function, while the latter used $Tanh(ax+b)$, where a and b are learnable parameters initialized to 0 and 1, respectively.

We evaluate the performance of the models using the relative L_2 -norm (Eq. 19) and measure the time per iteration in seconds with Python `time.time()` function. Table 3 shows the percentage errors and time metrics for each model.

$$\text{Relative } L_2 \text{ norm} = \frac{\|y - \hat{y}\|_2}{\|y\|_2} * 100\% \quad (19)$$

While the reported errors could be further optimized through more extensive hyperparameter tuning or an exhaustive architecture search, our focus is specifically on evaluating the models under consistent settings.

For simplicity, throughout the remainder of the paper, we refer to the models by their activation or basis function along with respective architecture identifier. For example, Tanh(A1) represents an MLP with Tanh activation function using A1 architecture, whereas B-spline(A2) represents KAN model with B-spline basis function using architecture A2.

Table 2 displays the two sets of architectures we utilized for evaluation, along with the total number of learnable parameters for each model. The hyperparameter settings of the KAN basis functions (see Table 1) used in the study are as follows: GRBF: $\sigma = 1$, $k = 8$; B-spline: $d = 3$, $k = 8$; Chebyshev: $d = 4$; Jacobi: $d = 4$, $\alpha = 1$, $\beta = 1$; Fourier:

Table 2

Two different neural network architectures (A1 and A2) and their corresponding parameters for MLP and KAN models across different scenarios exist. Architectures A1 and A2 differ in terms of the number of units (neurons) per layer and the overall network complexity. For the KAN in the A2 configuration, a reduced number of units is used to limit the total number of parameters, optimizing the model for computational efficiency. Cells marked with – indicate that a particular configuration or parameter was not used.

Arch	Case	Network	MLP		KAN				
			Tanh	Param-Tanh	B-spline	GRBF	Fourier	Chebyshev	Jacobi
A1	Helmholtz	[2, 30, 30, 30, 1]	1981	1983	18900	15120	15211	9450	9450
	Klein-Gordon	[2, 30, 30, 30, 1]	1981	1983	18900	15120	15211	9450	9450
	Wave	[2, 10, 30, 10, 1]	681	683	6300	5040	5091	3150	3150
	Convection-Diffusion	[3, 50, 50, 50, 1]	5351	5353	52000	41600	41751	26000	26000
	Cavity	[3, 50, 50, 50, 3]	5453	5455	53000	42400	42553	26500	26500
A2	Helmholtz	[2, 300, 300, 300, 1]	181801	181803	1809000	1447200	1448101	904500	904500
	Klein-Gordon	[2, 400, 400, 400, 1]	322401	322403	-	-	-	-	-
	Wave	[2, 300, 300, 300, 300, 1]	272101	272103	-	-	-	-	-
	Convection-Diffusion	[3, 300, 300, 300, 1]	182101	182103	-	-	-	-	-
	Cavity	[3, 300, 300, 300, 3]	182703	182705	-	-	-	-	-
	Klein-Gordon	[2, 200, 200, 200, 1]	-	-	806000	644800	645401	403000	403000
	Wave	[2, 150, 150, 150, 150, 1]	-	-	679500	543600	544201	339750	339750
	Convection-Diffusion	[3, 150, 150, 150, 1]	-	-	456000	364800	365251	228000	228000
	Cavity	[3, 100, 100, 100, 3]	-	-	206000	164800	165103	103000	103000

Table 3

Testing relative L_2 error (in %) for the cases considered in our study. We used two neural network architecture sets (A1 and A2), detailed in Table 2. The **lowest** and the **second-lowest** errors are highlighted. For simplicity, we select the best model based on the accuracy of the first feature in each row, which corresponds to the velocity u . Cells marked with – indicate that the error exceeded 90%. t/it : time per iteration in seconds.

Case		MLP				KAN									
		Tanh		param-Tanh		B-spline		GRBF		Fourier		Chebyshev		Jacobi	
		A1	A2	A1	A2	A1	A2	A1	A2	A1	A2	A1	A2	A1	A2
Helmholtz	u	6.13	6.62	5.51	4.52	1.93	3.03	17.9	8.11	3.09	–	5.17	–	19.5	–
	f	3.09	1.63	2.50	0.96	0.92	0.71	4.52	3.76	1.18	–	1.37	–	2.01	–
	t/it	0.0111	0.0116	0.0145	0.0153	0.0904	0.0907	0.0238	0.0243	0.0309	–	0.0934	–	0.1376	–
Klein-Gordon	u	1.58	9.48	11.4	18.6	5.23	13.2	15.0	25.8	9.25	–	12.7	–	8.36	–
	f	5.08	4.85	2.22	1.77	7.89	0.33	0.22	0.43	0.62	–	1.07	–	0.46	–
	t/it	0.0153	0.0131	0.0187	0.0154	0.1028	0.0841	0.0260	0.0254	0.0367	–	0.1044	–	0.1354	–
Wave	u	–	13.6	–	–	22.4	27.7	17.2	14.7	38.4	–	37.5	44.2	37.5	–
	t/it	–	0.0146	–	–	0.0823	0.1030	0.0217	0.0266	0.0294	–	0.0889	0.1167	0.1328	–
Convection Diffusion	u	12.6	13.6	12.1	11.6	11.7	12.3	11.5	12.8	15	–	17.5	–	29.9	–
	f	2.45	3.86	1.67	1.07	8.34	1.01	2.07	3.01	7.10	–	2.46	–	3.02	–
	t/it	0.0132	0.0170	0.0177	0.0174	0.0975	0.0991	0.0277	0.0299	0.0340	–	0.1005	–	0.1351	–
Cavity	u_x	13.9	10.8	13.5	15.7	7.87	4.09	13.1	13.5	25.2	40.9	17.2	14.6	16.9	37.1
	v_x	24.3	22.0	32.8	21.9	18.0	8.72	25.6	17.7	38.9	75.2	32.5	24.2	44.2	65.2
	p	25.9	24.4	45.8	33.5	25.4	21.3	28.2	29.7	52.2	–	37.1	52.2	54.1	–
	t/it	0.0282	0.0271	0.0333	0.0358	0.2030	0.1982	0.0537	0.0538	0.0771	0.0760	0.2137	0.2255	0.2923	0.2876

$k = 4$. Although an extensive hyperparameter search may uncover more optimal settings, these configurations were chosen to achieve optimal performance for moderately complex problems while minimizing the risk of overfitting and reducing computational complexity.

All experiments are performed on an NVIDIA A100 system consisting of a single node with 4 GPUs, each with 40 GB of VRAM. Measurements are taken on a single GPU with the same environment. Later, to accelerate training for Cavity, we used PyTorch’s Distributed Data-Parallel (DDP) framework to enable multi-GPU parallel training.

5.2. Results

The performance results, measured by relative L_2 error, for the different models and architectures across various test cases are summarized in Table 3. These results include comparing two architectures, A1 and A2, for the MLP using two types of activation functions: Tanh and parametric-Tanh. Additionally, the table presents the performance of KAN models using different basis functions: B-spline, GRBF, Fourier, Chebyshev, and Jacobi. This comparative analysis allows for evaluating how each architecture and activation function or basis function combination impacts model accuracy under consistent test conditions.

Table 4

The table presents a comparison of the final training losses for MLP and KAN models across two architectures and selected PDEs. The training losses include L_{phy} , representing the physics-informed loss related to the PDE; L_{bc} , which denotes the boundary conditions loss; and L_{ic} , which corresponds to the initial conditions loss. Further details regarding these loss functions are provided in Sec. 4.

Case		MLP				KAN									
		Tanh		param-Tanh		B-spline		GRBF		Fourier		Chebyshev		Jacobi	
		A1	A2	A1	A2	A1	A2	A1	A2	A1	A2	A1	A2	A1	A2
Helmholtz	L_{phy}	4.4e+00	1.91e+00	2.04e+00	2.4e-01	6.1e-01	2.75e-01	1.04e+01	2.7e+00	1.0e+00	3.30e+12	8.3e-01	7.15e+03	2.9e+00	6.80e+03
	L_{bc}	6.6e-03	3.27e-03	6.55e-03	3.1e-03	1.5e-03	1.66e-03	1.30e-02	2.1e-02	2.7e-03	3.39e-01	2.8e-03	1.13e-01	2.3e-02	1.50e-01
Klein-Gordon	L_{phy}	1.9e-01	8.57e+00	1.3e+00	1.31e+00	3.0e-01	2.01e-01	1.2e-01	2.64e-01	4.6e-01	2.29e+06	2.4e+00	1.19e+04	3.5e-01	9.46e+03
	L_{bc}	6.0e-05	3.86e-04	7.4e-04	7.39e-04	4.2e-05	1.00e-05	2.5e-05	4.74e-04	5.7e-04	5.96e-01	8.6e-04	4.16e-02	3.9e-04	5.21e-02
	L_{ic}	4.5e-06	4.74e-04	7.5e-05	7.47e-05	4.8e-06	4.34e-06	6.1e-06	4.83e-04	8.1e-05	3.30e-01	6.6e-05	2.32e-01	4.3e-04	1.82e-01
Wave	L_{phy}	1.47e-01	1.2e-01	3.24e-02	3.7e-02	3.1e-02	3.00e-02	8.83e-01	6.6e-01	1.3e+00	1.65e+10	2.9e-01	3.77e-01	8.9e-01	1.89e-07
	L_{bc}	1.46e-02	4.3e-04	1.09e-02	1.7e-04	5.0e-05	2.74e-05	1.45e-03	1.6e-03	1.3e-02	9.30e-02	1.5e-02	3.50e-02	1.8e-02	5.97e-02
	L_{ic}	3.54e-03	7.8e-05	4.59e-03	3.6e-05	7.6e-06	9.23e-06	6.64e-04	5.8e-04	1.3e-02	3.92e-01	3.2e-03	1.15e-02	7.7e-03	4.50e-01
Convection Diffusion	L_{phy}	7.2e-04	1.74e-03	2.74e-04	5.8e-03	6.0e-05	5.30e-05	2.7e-04	7.28e-03	6.3e-03	5.52e+05	1.1e-03	1.02e+00	8.5e-04	9.69e-01
	L_{bc}	3.0e-05	3.16e-05	2.15e-05	2.6e-05	8.3e-06	2.28e-05	2.3e-05	4.39e-05	1.3e-04	4.50e-03	1.6e-04	1.02e-02	8.6e-04	3.67e-05
	L_{ic}	5.4e-05	8.99e-05	7.77e-05	1.2e-04	5.3e-06	4.31e-06	6.3e-05	7.21e-05	1.3e-04	1.37e-02	1.2e-04	8.87e-03	4.2e-04	1.61e-02
Cavity	L_{phy}	1.42e-01	2.2e-02	1.3e-01	2.79e-02	2.56e-01	2.3e-02	1.4e-01	6.75e-02	2.1e-01	3.25e-01	1.34e-01	2.9e-02	2.4e-01	1.86e-07
	L_{bc}	1.35e-02	4.5e-04	3.4e-04	1.08e-02	2.95e-03	1.5e-05	4.4e-03	5.06e-03	3.6e-03	1.50e-02	1.39e-02	1.4e-03	9.1e-03	1.02e+00
	L_{ic}	2.57e-03	6.6e-03	4.0e-03	3.81e-03	6.53e-04	2.5e-04	5.7e-03	4.57e-03	7.6e-03	1.04e-02	3.81e-03	3.7e-03	6.7e-03	8.42e-02

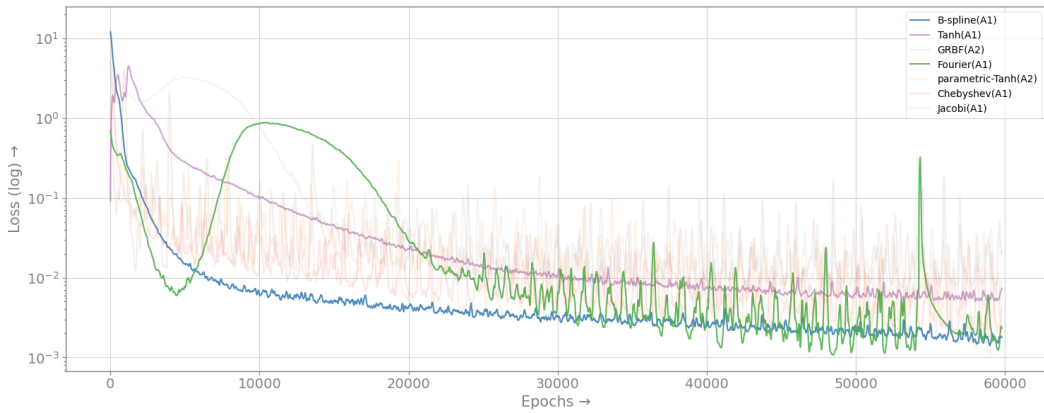


Figure 2: Training convergence history for the Helmholtz equation. The loss curves for all models are shown, with **B-spline(A1)**, **Fourier(A1)**, and **Tanh(A1)** highlighted in saturated colors, which demonstrated the best convergence behavior. The remaining models are depicted with transparency to enhance visual distinction and clarity.

5.2.1. Helmholtz Equation

Fig. 2 shows the training loss, i.e., convergence history for the best-performing architectures from each model group from Table 3. The plot indicates that both Tanh(A1), Fourier(A1), and B-spline(A1) exhibit relatively better convergence compared to other models. While B-spline(A1) and Tanh(A1) demonstrate stable training dynamics with smooth loss reduction, the other models show relatively unstable behaviors, characterized by persistent fluctuations throughout the training process. Ultimately, B-spline(A1) achieves the lowest final loss value of $1.5e - 03$, $6.1e - 01$ for the L_{bc} , L_{phy} respectively, while Fourier(A1) and Tanh(A1) stabilize at loss value of $2.7e - 3$, $1.0e + 00$ for the L_{bc} , L_{phy} and $6.6e - 03$, $4.4e + 00$ for the L_{bc} , and L_{phy} , respectively. For this problem, it is observed that adding more weights to the boundary condition loss term guarantees better results. This is reflected in the high training error on the physics loss term compared to the boundary loss term in all models. Yet, the physics loss term is necessary as a regularizer. This also signifies the critical importance of designing the loss function in PINN regardless of the neural network architecture used.

The training convergence of B-spline(A1) and Fourier(A1) closely reflects their better performance during testing.

All models using Tanh and parametric-Tanh activation functions demonstrate similar accuracy, with velocity errors 4.5 – 6.6 % and force errors 1.0 – 3.1%. The results indicate that increasing the number of neurons does not significantly improve the performance of either Tanh or parametric-Tanh activations. Among KAN models, B-spline(A1) achieves

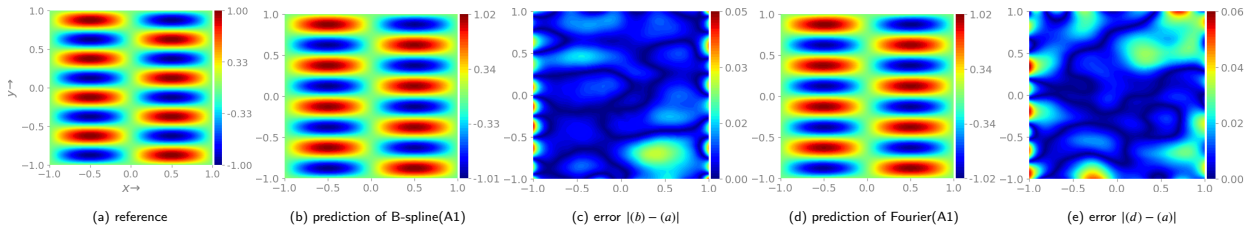


Figure 3: Contour plots for the solution of the Helmholtz equation. The plots depicts the reference or actual solution, the predicted solution, and the corresponding error for the two best-performing models identified in Table 3. (b) presents the prediction of **B-spline(A1)** model, which achieves the lowest error of 1.93%, while (d) shows the prediction of **Fourier(A1)** model, which has a relative error of 3.09%.

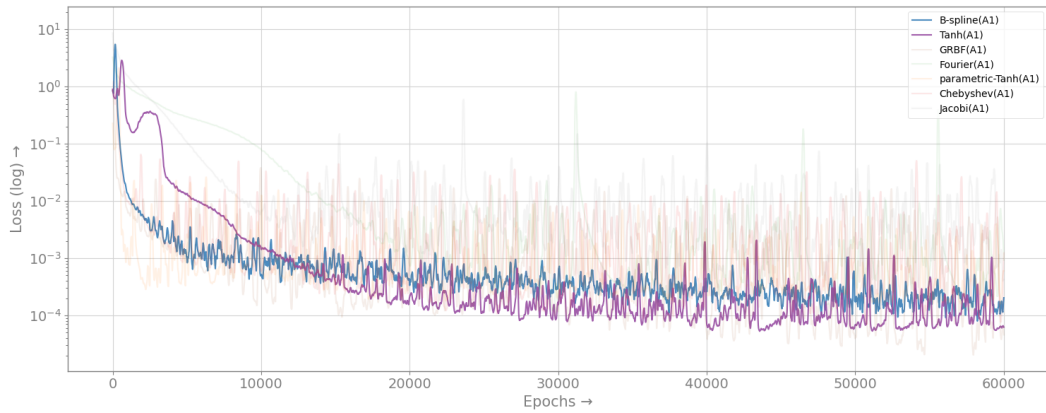


Figure 4: Training convergence history for the Klein-Gordon equation. The loss curves for the two best converging models, **Tanh(A1)** and **B-spline(A1)**, are highlighted.

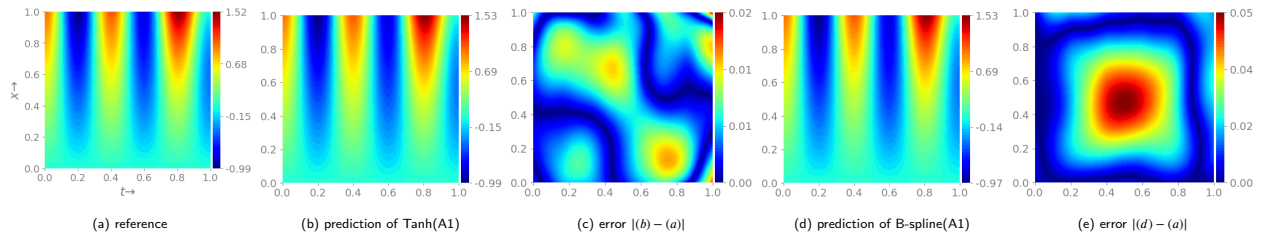


Figure 5: Contour plots for the solution of the Klein-Gordon equation. The plots depicts the reference or actual solution, the predicted solution, and the corresponding error for the two best-performing models identified in Table 3. (b) presents the prediction of **Tanh(A1)** model, which achieves the lowest error of 1.58%, while (d) shows the prediction of **B-spline(A1)** model, which has a relative error of 5.23%.

the lowest velocity error of 1.9% with a corresponding force error 0.9%, followed closely by Fourier(A1), which yields a velocity error 3.0% with a corresponding force error 1.1%. In contrast, GRBF(A1) and Jacobi(A1) result in significantly higher errors, 17.9% and 19.5% respectively. Fourier(A2), Chebyshev(A2), and Jacobi(A2) exhibit instability, with errors exceeding 90.0%, indicating failure in these cases.

Fig. 3 compares the reference solution and the predicted solutions from B-spline(A1) and Fourier(A1) for the Helmholtz equation. The majority of inference errors for both models are concentrated near the boundaries of the domain, with Fourier model showing more pronounced deviations in these regions. This could be attributed to the oscillatory nature of Fourier basis functions, which may introduce additional errors near the domain boundaries, making accurate approximation more challenging.

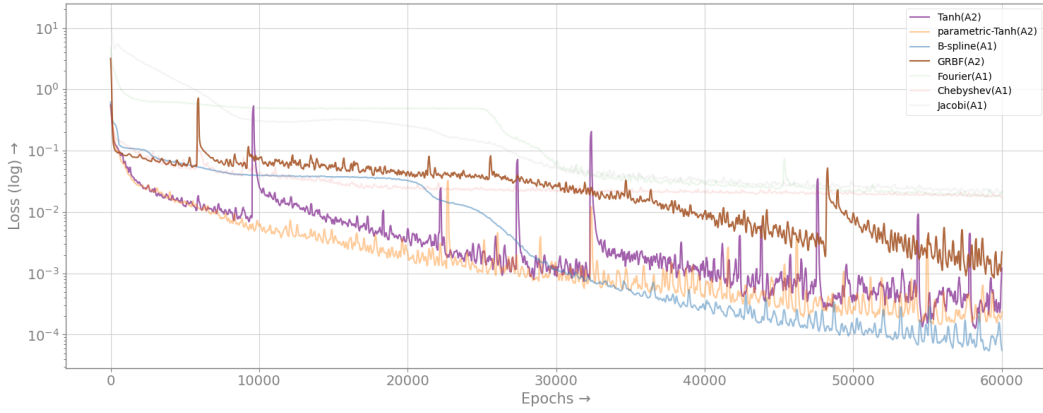


Figure 6: Training convergence history for the Wave equation. The loss curves indicate that **B-spline(A1)** and **parametric-Tanh(A2)** models exhibit the most consistent convergence. However, **Tanh(A2)** and **GRBF(A2)** models achieve the lowest testing errors, as reported in Table 3.

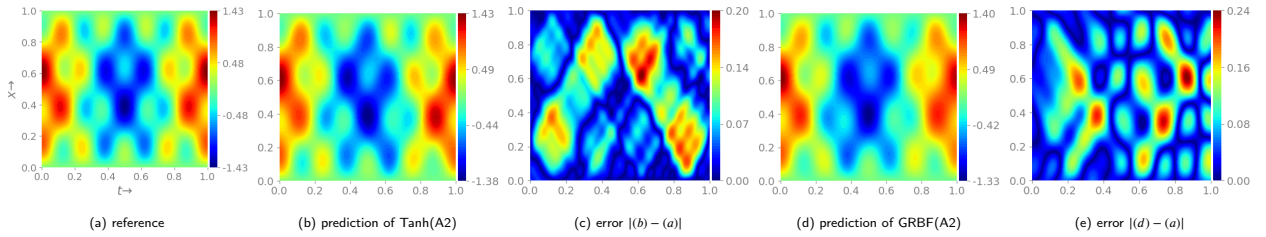


Figure 7: Contour plots for the solution of the Wave equation in the spatio-temporal domain x . The plots depicts the reference or actual solution, the predicted solution, and the corresponding error for the two best-performing models identified in Table 3. (b) presents the prediction of **Tanh(A2)** model, which achieves the lowest error of 13.6%, while (d) shows the prediction of **GRBF(A2)** model, which has a relative error of 14.7%.

5.2.2. Klein-Gordon Equation

Table. 3 shows that increasing the number of neurons from A1 to A2 leads to degradation in velocity prediction across all models. The **Tanh(A1)** achieves the lowest velocity error at 1.58%, with a corresponding force error of 5.08%, followed by **B-spline(A1)**, which results in a velocity error of 5.23% and force error 7.89%. Like in the Helmholtz case, the **Fourier(A2)**, **Chebyshev(A2)**, and **Jacobi(A2)** methods exhibit instability, with errors exceeding 90.0%, indicating failure.

Fig. 4 shows the training convergence history of Klein-Gordon equation. **Tanh(A1)** achieved the lowest relative error for the velocity. Meanwhile, the **B-spline(A1)** shows a more stable convergence with minimal fluctuations, reflecting steady learning throughout training. Other models also display instability and oscillatory behavior, suggesting challenges in optimizing the solution for the Klein-Gordon equation under the given settings. The **Tanh(A1)** and **B-spline(A1)** stabilize at 0.063 and 0.1 total training loss, respectively. The training convergence of **Tanh(A1)** and **B-spline(A1)** closely reflects the performance during testing, demonstrating a consistent relationship between training stability and testing accuracy.

Fig. 5 shows the solution of the Klein-Gordon equation's solution in the spatio-temporal domain $x \in [0, 1], t \in [0, 1]$, comparing the reference solution to the best-predicted solutions from **Tanh(A1)** and **B-spline(A1)**, alongside the corresponding error plots. Both models exhibit error concentration in regions with high gradients, where the solution changes rapidly. However, the **Tanh(A1)** manages these high-gradient areas more effectively, as evidenced by the lower overall error in Fig. 5(c) compared to the error observed for the **B-spline** results in Fig. 5(e).

5.2.3. Wave Equation

The **Tanh(A2)** model achieves the lowest velocity error at 13.6%, followed by **GRBF(A2)**, which has a velocity error of 14.7% (as in Table 3). **B-splines**, **Fourier**, **Chebyshev**, and **Jacobi** models capture the general structure of the

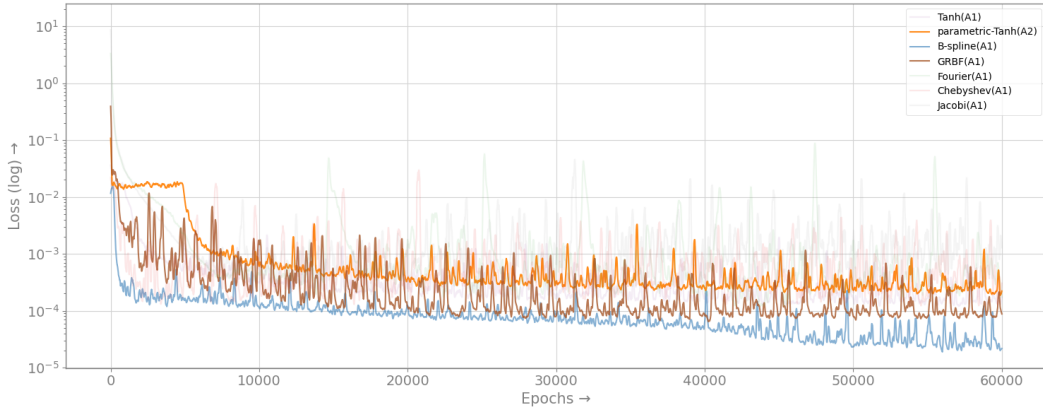


Figure 8: Training convergence history for the Convection-diffusion equation. The loss curves for all models are displayed, with **B-spline(A1)**, **GRBF(A1)**, and **parametric-Tanh(A2)** demonstrated the best convergence.

wave solution with errors ranging from 22.4% to 44.2%, which may suggest that the models are underfitting or failing to capture finer details in the solution. More specifically, they fail to accurately capture the higher-frequency components of the solution, especially around the boundaries.

Fig. 6 presents the training convergence history for the Wave equation. The plots indicate that B-spline(A1), parametric-Tanh(A2), Tanh(A2), and GRBF(A2) demonstrate better convergence. The B-spline(A1) model experienced a slower convergence rate during the initial half of the training period, after which it began to converge more rapidly, ultimately reaching the lowest loss value. The parametric-Tanh(A2) showed steady convergence, while both Tanh(A2) and GRBF(A2) exhibited some fluctuations throughout the training process. Ultimately, B-spline(A1), parametric-Tanh(A2), Tanh(A2), and GRBF(A2) stabilize at 0.01, 0.012, 0.04 and 0.22, respectively. Although B-spline(A1) and parametric-Tanh(A2) achieve the fastest convergence and lowest final loss values during the training, the test results, as shown in Table 3, indicate that Tanh(A2), and GRBF(A2) deliver lower relative errors.

Fig. 7 shows the contour plot predictions for the velocity fields using Tanh(A2) and GRBF(A1). Tanh(A2) effectively captures the continuous dynamics of the wave. The GRBF(A1) model has a slightly higher relative error than Tanh(A2), with most errors concentrated in the regions where the wave oscillates rapidly. This suggests that GRBF struggles to accurately approximate the steep gradients in these solution regions.

5.2.4. Convection-diffusion Equation

The GRBF(A1) model achieves the lowest velocity u with error of 11.5%, followed by parametric-Tanh(A2) with a velocity error of 11.6% (as in Table 3). For the force term f , the B-spline(A2) model performs best, achieving an error of 1.01%. In contrast, Fourier, Chebyshev, and Jacobi models exhibited high errors with the A1 architecture and failed to converge effectively with A2.

Fig. 8 presents training convergence history for the Convection-diffusion equation. The plots indicate that B-spline(A1), GRBF(A1), and parametric-Tanh(A2) exhibit better convergence compared to other models. The B-spline(A1) model demonstrates the most consistent convergence, characterized by smooth loss reduction with minimal fluctuations throughout the training. In contrast, the GRBF(A1) model shows less stability and more noticeable fluctuations. The B-spline(A1) model also achieves the fastest initial convergence, with a significant reduction in loss within the first few epochs, whereas GRBF(A1) and parametric-Tanh(A2) demonstrates more gradual declines. While some oscillations are observed across all three models during training, these are notably less pronounced than in other cases. The remaining models display considerable instability, evidenced by pronounced oscillations in their loss curves. Ultimately, B-spline(A1), GRBF(A1), and parametric-Tanh(A2) stabilize at 2.45×10^{-5} , 1.18×10^{-4} and 0.002×10^{-4} , respectively. Although, B-spline(A1) achieves the fastest convergence and lowest final loss value, the test results, as summarized in Table 3, indicate that GRBF(A1) and parametric-Tanh(A2) deliver lower relative errors.

Fig. 9 presents the solution of the Convection-Diffusion equation for the velocity and the force values at the beginning and the end of the simulation using parametric Tanh(A2) and the GRBF(A1) models. The reference velocity is concentrated in the center (0.5, 0.5) at time step 0, dissipating as time progresses (shown by the shrinking central

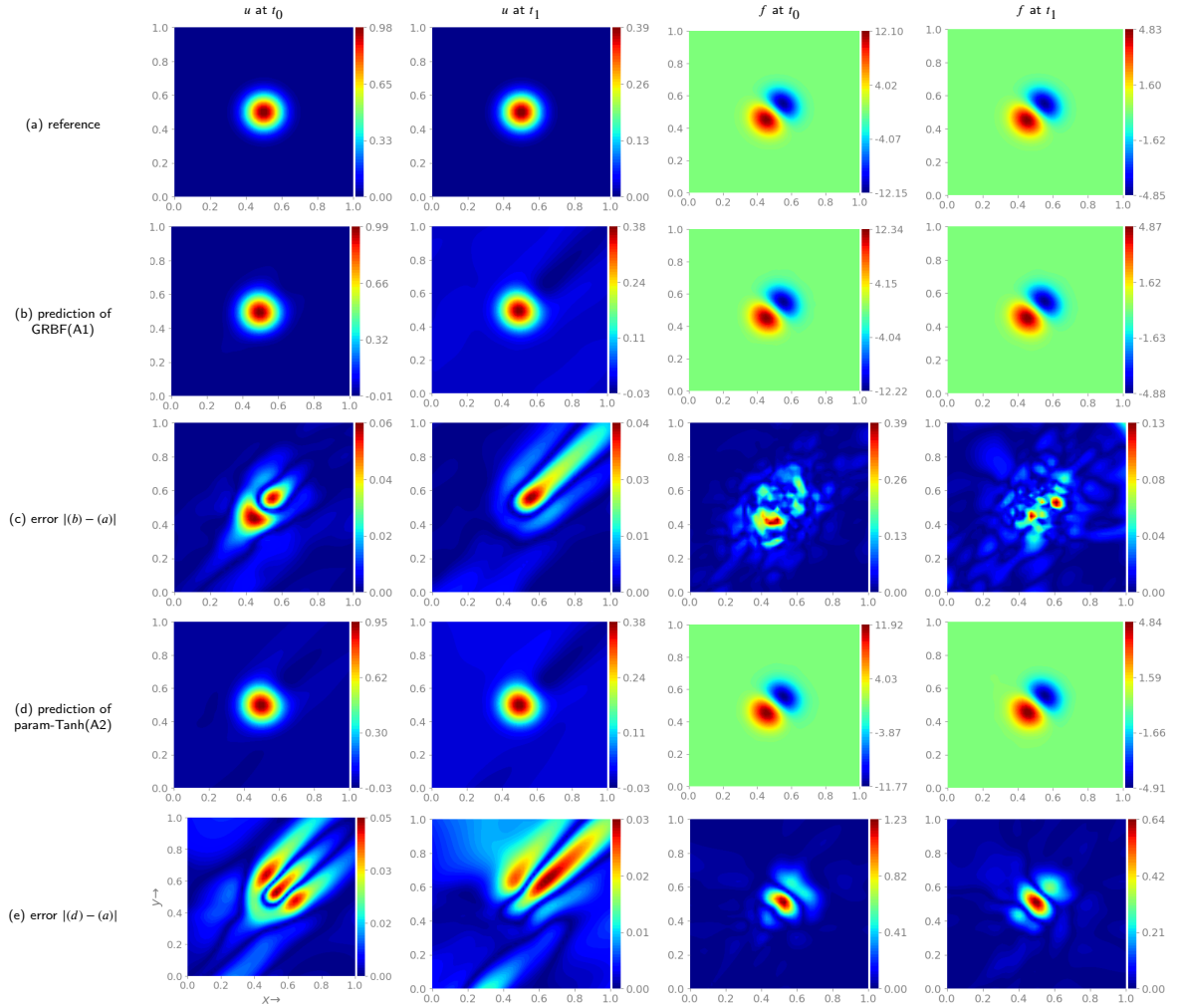


Figure 9: Contour plots for the solution of the Convection-diffusion velocity (v) and force (f) values at time-step zero (t_0) and one (t_1) in the spatio-temporal domain. The plots at each row depict the reference or actual solution, the predicted solution, and the corresponding error for the two best-performing models identified in Table 3, respectively. (b) presents the prediction of GRBF(A1) model, the relative L_2 errors at t_0 are 11.5% 2.07% for u and f , respectively. (d) presents the prediction of parametric-Tanh(A2) model, the relative L_2 errors at t_0 are 11.6% 1.07% for u and f , respectively. Note that only the result of t_0 is recorded in Table 3, results of t_1 can be reproduced using the pretrained model provided with our source code.

area at time step 1). Similarly, the force field is shown in the third and fourth columns, with the high-intensity areas at time-step 0 diffusing over time.

In the second row of Fig. 9, the GRBF model captures the dissipation of the velocity field reasonably well, with only minor errors (as seen in the error plot in row (c)). Similarly, for the force field, the GRBF model captures the general diffusion pattern accurately, with relatively low errors (compared to other models).

Parametric Tanh(A2) has a slightly higher relative error for velocity (11.6%) and a lower error for force (1.07%). The error plots show that while the model is competitive, it does not precisely capture the initial sharp gradients as GRBF(A1).

5.2.5. Cavity Equation

Table 3 presents the testing errors for the Cavity problem. The B-spline(A2) model achieves the lowest errors, with relative L_2 errors of 4.1%, 8.7% and 21.3% for u_x , v_x and p_x respectively. This is followed by Tanh(A2), which

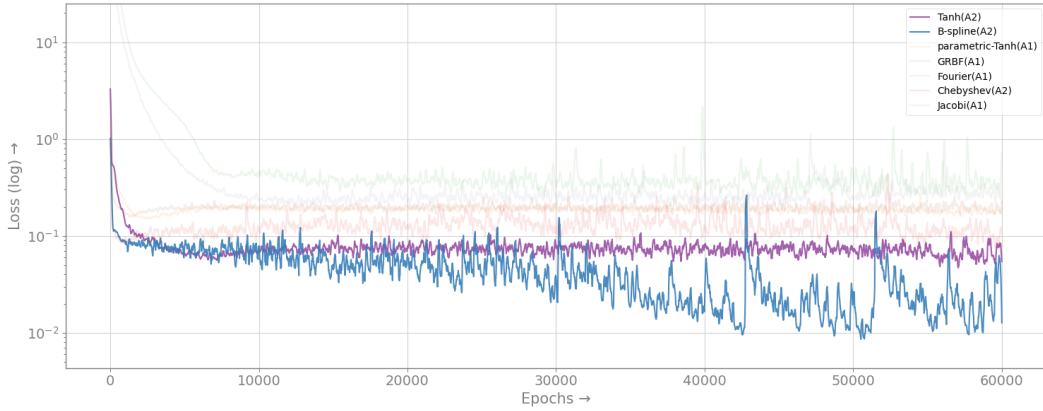


Figure 10: Training convergence history for the Cavity problem. Loss curves for all models are shown, with **B-spline(A2)** and **Tanh(A2)**, which demonstrated the best convergence.

results in error of 10.8%, 22%, 24.4% for the u_x , v_x and p_x respectively. In contrast, the Fourier, Chebyshev, and Jacobi perform less effectively for the Cavity problem, showing significantly higher errors, especially for the pressure field and velocity components, with errors exceeding 30% across all models.

Fig. 10 shows training convergence history for the Cavity problem. The B-spline(A2) model demonstrates the most effective convergence, starting from a relatively high initial loss but rapidly decreasing, ultimately settled at a low value. However, B-spline(A2) exhibits relatively unstable behaviors, characterized by persistent fluctuations throughout the training process. The Tanh(A2) model achieves early stabilization, with its loss curve flattening quickly and remaining consistent for the remainder of the training iterations – a pattern observed similarly in other remaining models. Ultimately, B-spline(A2) achieves the lowest final total loss value of 0.0077, indicating the most effective convergence, while Tanh(A2) settles at 0.0096 total training loss after 60,000 iterations.

Fig. 11 shows the solution of the cavity problem, comparing the reference solution to predictions made by B-spline(A2) and Tanh(A2) at the initial Cavity flow time step (t_0) over the spatio-temporal domain $x \in [0, 1]$, $t \in [0, 10]$. The predicted u_x field by the Tanh(A2) is mostly close to zero, as expected for the time step 0, but there are slight deviations at the bottom. However, the v_y field shows deviations from the reference. It exhibits sharp gradients along the top boundary and misrepresentations at the center, leading to visible errors, which explains the high relative error of 22% from the table. The smooth nature of the Tanh activation seems to struggle to capture the sharp boundary behavior accurately. The pressure field predicted by the Tanh(A2) has significant deviations, particularly near the top boundary. The reference pressure is zero, but the predicted pressure is around 0.06, leading to a high relative error of 24.4%. There are some deviations in the B-spline(A2) model, but the overall structure is closer to the reference solution.

Fig. 12 shows the plots of the reference solution, the Tanh, and the B-spline approximations when solving the cavity problem at time-step zero and ten. The Tanh(A2) model reasonably approximates u_x field, showing a similar pattern to the reference solution with high velocities near the top boundary. However, the velocity distribution near the bottom of the cavity has more deviation from the reference. The v_y field shows noticeable differences compared to the reference, particularly in the location and shape of the recirculating flow. The recirculation is weaker and more diffuse than the reference solution, leading to higher errors. The pressure field predicted by the Tanh(A2) model shows a significant deviation from the reference. There is a visible misrepresentation of the pressure distribution, particularly along the top boundary, where the pressure gradients are not well captured.

5.2.6. Computational Complexity

Table 3 shows the time required for training in seconds per iteration for each model. The number of parameters for MLP models is much lower than that of KAN models for basis functions (e.g., B-splines or other polynomials) and possibly extra weights for handling those functions (as shown in Table 2). MLP with Tanh activation functions, followed by GRBF, generally have lower times per iteration (t/it), while KAN with Jacobi basis function tends to have the highest computational cost compared to other models

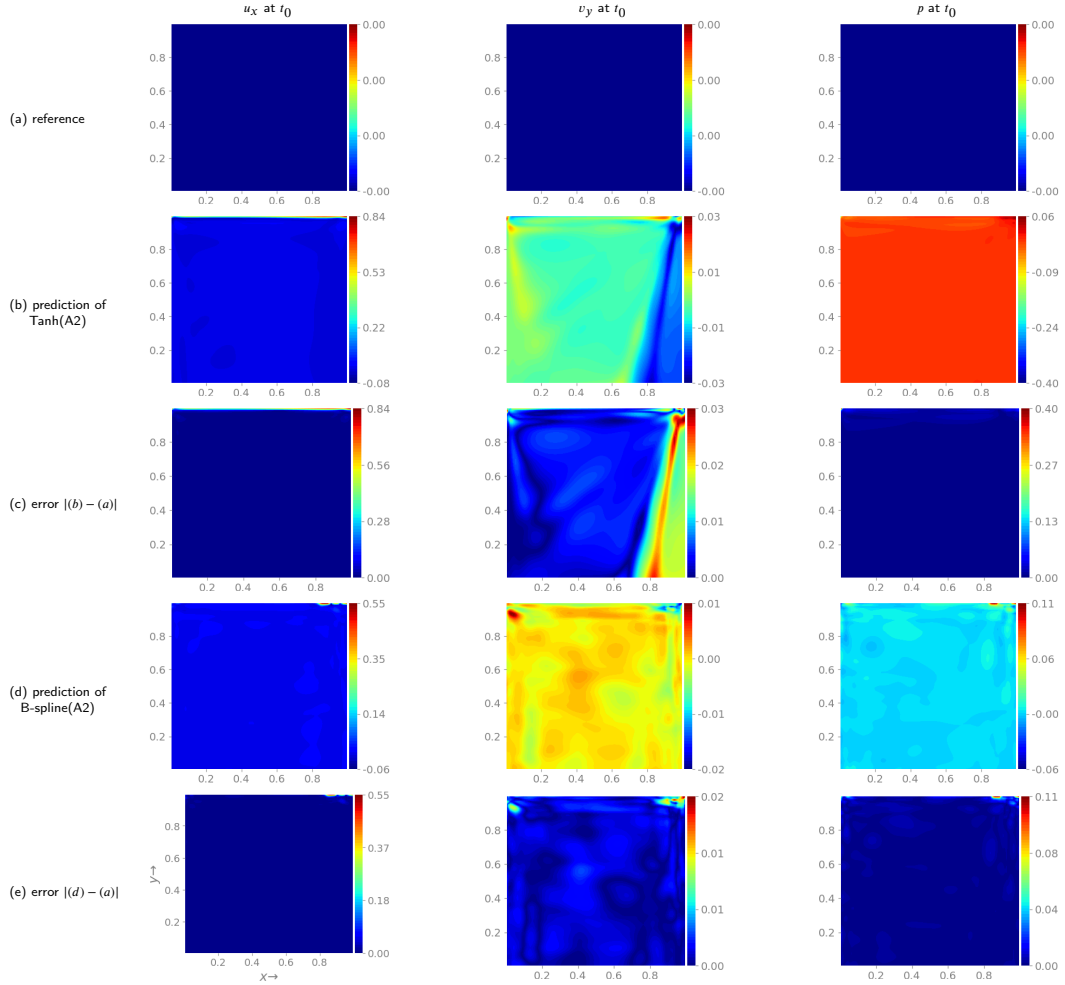


Figure 11: Contour plots for the solution of the Cavity problem velocity (u_x and v_y) and pressure (p) values at time-step zero (t_0), with $Re = 100$. (b) presents the prediction of **Tanh(A2)** model, the relative L_2 errors as 10.8%, 22%, and 24.4% for u_x , v_y , and p , respectively. (d) presents the prediction of **B-spline(A2)** model, the relative L_2 errors are 4.1%, 8.7%, and 21.3% for u_x , v_y , and p , respectively.

The relatively small increase in time per iteration, despite the larger parameter count in architecture A2 compared to architecture A1, is likely a result of the NVIDIA A100’s parallel processing capabilities and efficient utilization of optimizations in PyTorch. Furthermore, 128 batch size balances computational efficiency and memory usage. Since the same minibatch size is used for both A1 and A2 architectures, the increased parameter count in A2 may not be sufficient to cause significant changes in time per iteration.

5.2.7. Convergence analysis and Spectral Bias

In the following sections, we analyze the behavior of the maximum eigenvalue of the loss Hessian over the course of training epochs. These experiments employed the Adam optimizer, configured with a learning rate of 0.001 and a weight decay of 10^{-6} . In addition, mini-batch gradient descent was utilized with a batch size of 128.

Fig. 13 presents the maximum eigenvalue of the Hessian of the loss function, denoted as $\lambda_{max}(\nabla_{\theta}^2 \mathcal{L})$. The Hessian matrix consists of the second-order partial derivatives of the loss function with respect to model parameters. The largest eigenvalue of this Hessian matrix is estimated as a Rayleigh quotient using the power iteration method[30, 63]. The Hessian matrix provides valuable insights into the curvature of the loss landscape, and analyzing its eigenvalues can offer a critical understanding of the learning dynamics and optimization stability of the best-performance network

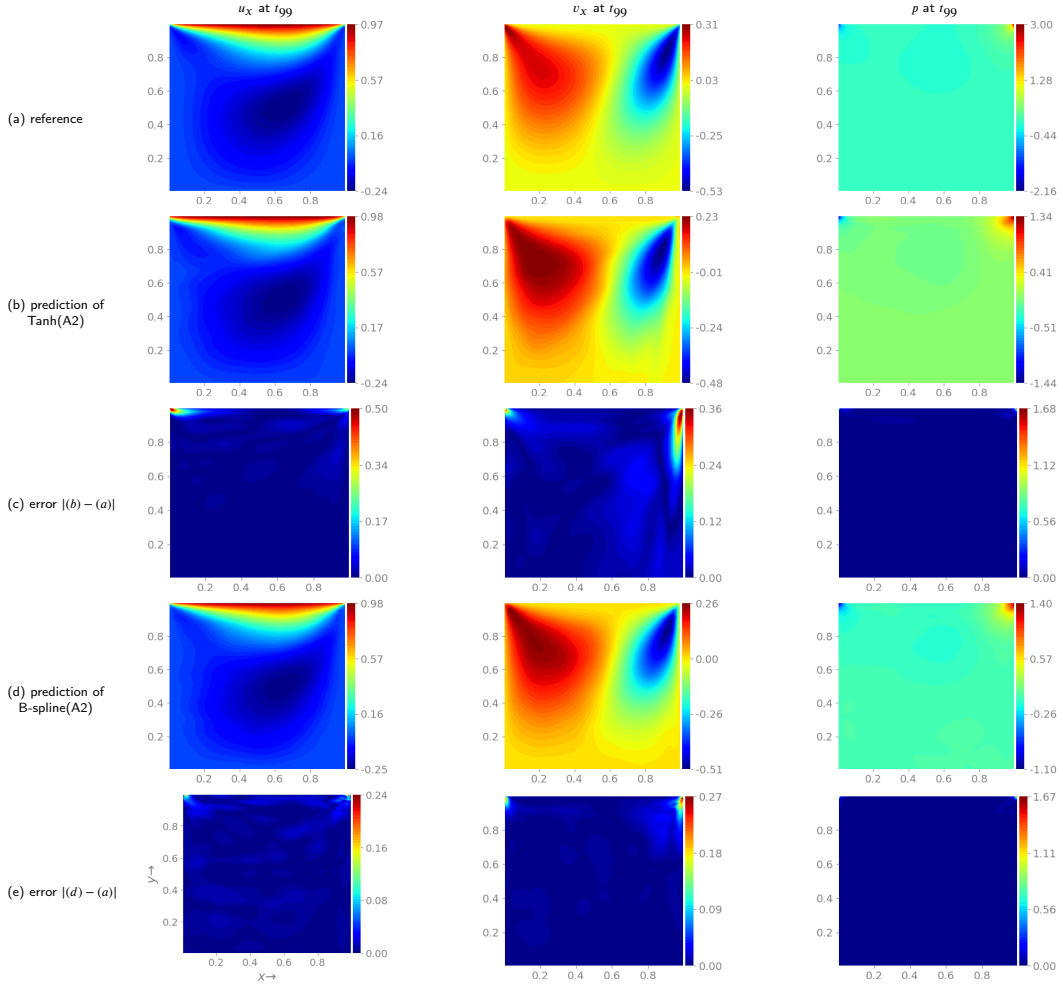


Figure 12: Contour plots for the solution of the Cavity problem, showing velocity components (u_x and v_y) and pressure (p) values at time-step 99 (t_{99}), with $Re = 100$. (b) shows the prediction from the **Tanh(A2)** model, with relative L_2 errors of 10.8% 22% 24.4% for u_x , v_y , and p , respectively. (d) shows the prediction from the **B-spline(A2)** model, which achieved relative L_2 errors of 4.1%, 8.7%, 21.3% for u_x , v_y , and p , respectively. Note that only the result of t_0 is recorded in Table 3, results of t_{99} can be reproduced using the pretrained model provided with our source code.

architectures [14]. In particular, larger eigenvalues can create challenges during the training process [30]. The behavior and fluctuations of λ_{max} reveal how well each neural network architecture and basis function manages the spectral bias issue. By plotting λ_{max} across training epochs, we can assess the effectiveness of various architectures and basis functions in addressing spectral bias during learning.

Tanh and parametric-Tanh activations. MLPs using Tanh or parametric-Tanh activations typically exhibit a preference for learning low-frequency components first. This phenomenon is evident in the initial stability of λ_{max} observed across multiple cases, such as the Helmholtz and Klein-Gordon equations, see Fig. 13 (a) and (b). As training progresses, the slow stabilization of λ_{max} suggests the delayed learning of high-frequency components.

Fluctuations in λ_{max} for parametric-Tanh activation, especially in the physics loss Hessian $\nabla_{phy}^2 \mathcal{L}$, suggest that while the network initially learns smooth, low-frequency features, it struggles with capturing high-frequency features. **B-spline basis function.** KAN with B-spline basis function consistently shows lower and more stable λ_{max} values, indicating a smoother optimization process with minimal spectral bias. B-splines, due to their flexibility, excel at representing both low- and high-frequency components without avoiding the bias towards either. This is corroborated by the performance results discussed earlier, where B-spline achieve the lowest error rates and demonstrated steady

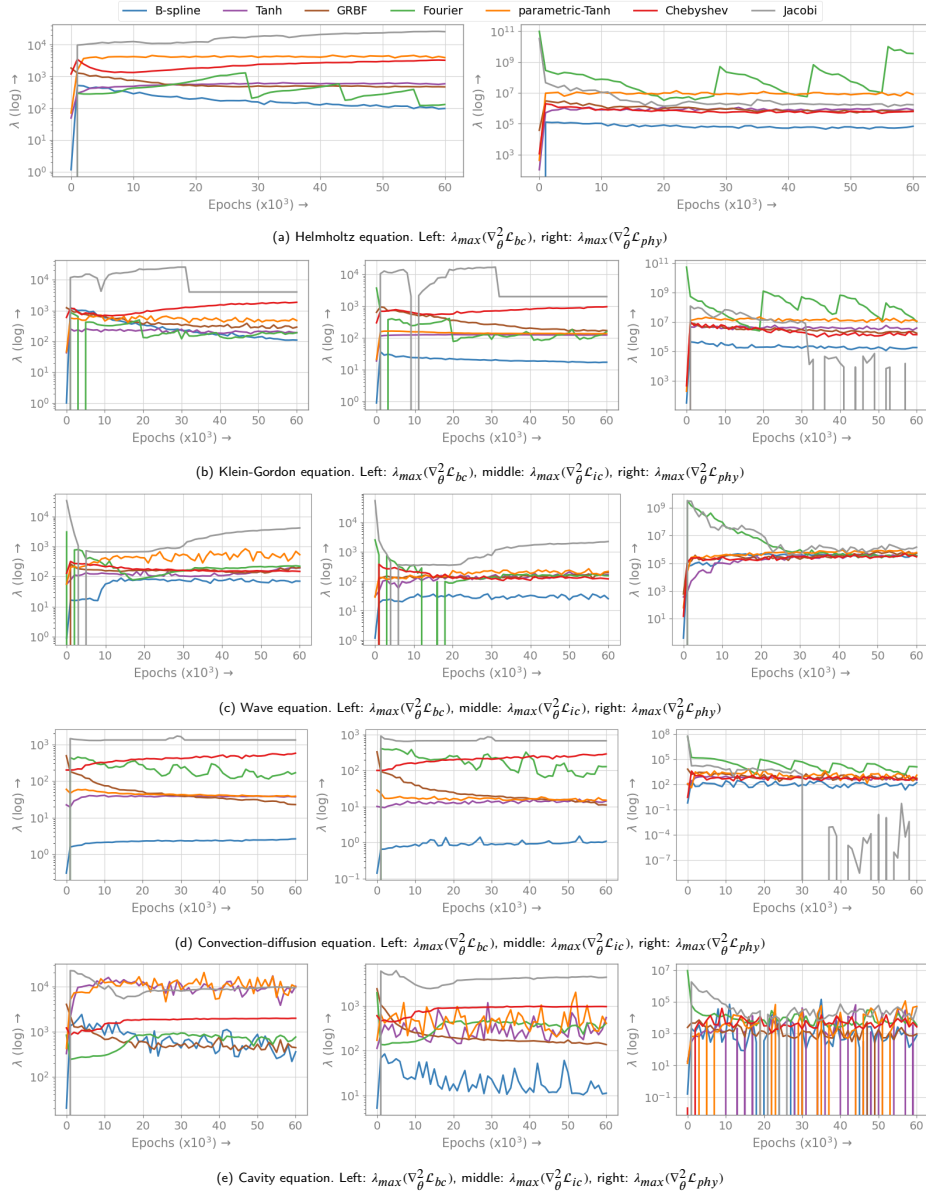


Figure 13: Evolution of the maximum eigenvalue of the Hessian of the loss function, λ_{\max} , over training epochs for different neural network architectures. The eigenvalue behavior illustrates the learning dynamics and spectral bias handling of Tanh, parametric-Tanh, B-spline, GRBF, Fourier, Chebyshev, and Jacobi basis functions. Significant fluctuations in λ_{\max} are observed, especially in the physics loss term.

convergence across various test cases. Furthermore, the stability of B-splines in learning both boundary and initial condition suggests that this architecture effectively manages spectral bias and captures high-frequency components early in the training process.

GRBF and Fourier basis functions. GRBF and Fourier basis functions initially exhibit some instability as seen in the fluctuating λ_{\max} , but eventually stabilize. This pattern suggests while these basis functions might struggle with spectral bias first, they adapt quickly compared to Tanh-based architectures. Fourier basis functions are naturally well-suited for representing periodic, high-frequency components, yet the observed fluctuations in λ_{\max} indicate some difficulty in balancing learning of low- and high-frequency features.

Chebyshev and Jacobi basis functions. The Chebyshev and Jacobi basis functions show significant instability, as reflected in their fluctuating λ_{max} values, particularly in the Cavity and Convection-diffusion cases. This instability suggests a strong bias towards certain frequencies or difficulty in learning high-frequency features, as confirmed by their higher error rates and unstable convergence seen in the loss history figures. For the Jacobi basis function, in particular, the large fluctuations in λ_{max} , especially in the physics loss term, indicate significant difficulties in handling high frequencies, which corresponds with poor performance in many test cases.

Physics loss Hessian ($\lambda_{max}(\nabla_{\theta}^2 \mathcal{L}_{phy})$). Fig. 13 shows that the maximum eigenvalue of the physics loss consistently takes longer to stabilize and are generally larger than the eigenvalues of the boundary and initial condition losses, even for more stable basis functions like B-splines. This discrepancy arises from the physics loss Hessian encoding more complex, high-frequency information and applying across the entire problem domain, often with more training datasets than other terms. As a result, the physics loss tends to exhibit numerical stiffness, leading to larger eigenvalues and slower convergence.

In cases, e.g., Helmholtz, Klein-Gordon, and Cavity problems, the fluctuations in the physics loss Hessian are particularly pronounced. Moreover, the presence of negative eigenvalues in the physics loss Hessian, as observed in Convection-diffusion and Cavity problems, highlights the challenging optimization landscape for the physics loss compared to the boundary and initial condition losses. The appearance of negative curvature further indicates that gradient-based optimizers, such as Adam, may struggle in these cases, as they are better suited for convex optimization problems. Negative curvature can cause optimization algorithms to get trapped in saddle points or lead to slower convergence. Recent studies such as Rathore et al., [37], suggest Newton’s method or preconditioned gradient descent techniques can help navigate these regions by using second-order information to escape saddle points and improve convergence rates.

6. Discussion

For simpler problems, e.g., Helmholtz and Klein-Gordon experimental results indicate that increasing the network size or number of learnable parameters (Table 2) leads to decreased performance (Table 3), likely due to training instability. Models with a large number of trainable parameters often suffer from vanishing gradient problems, particularly when using high-order polynomials as basis functions, e.g., Chebyshev.

KANs exhibit higher effectiveness when employed in simpler network architectures like A1, particularly for problems characterized by smooth and globally defined features. However, they encounter significant difficulties managing the increased complexity introduced in more sophisticated architectures, such as A2, especially for problems requiring precise local adjustments. Conversely, for complex problems, e.g., Cavity with large number of parameters, KAN demonstrate improved performance, achieving approximately 3% accuracy improvement.

The Tanh activation achieves higher accuracy when applied to Klein-Gordon and Wave equations and reasonably well on the remaining cases. The Helmholtz, Klein-Gordon, and Wave equations represent second-order partial differential equations describing wave phenomena. The smoothness of the Tanh function appears to align well with the underlying characteristics of these equations, enabling the PINNs to approximate them effectively. Despite the expectation of improved performance, the parametric-Tanh activation underperformed and failed to solve the Wave equation, perhaps due to the sensitivity of trainable activation to hyperparameter choices. Thus, choosing an activation function, whether fixed or trainable, is still problem-dependent.

Basis functions like B-splines and GRBF solved all the cases with lower errors, suggesting that their use within KANs can significantly enhance model accuracy, particularly when addressing problems with localized features or high variability. Due to their piecewise polynomial construction, B-splines are effective for modeling localized features of the solution. This characteristic is advantageous when approximating PDEs with sharp gradients or boundary layers, such as those present in the Convection-diffusion equations. Their local support properties contribute to reducing global oscillations, enabling more precise modeling of complex local behaviors.

In contrast, Fourier basis functions, owing to their global nature, influence the entire domain, limiting their ability to capture local variations. This characteristic often leads to slower convergence for problems with non-periodic or complex boundary conditions. For problems involving sharp transitions, such as the Wave or Cavity problems, the Fourier basis struggles to accurately approximate the solution, often resulting in oscillatory behavior near discontinuities (commonly referred to as the Gibbs phenomenon), which explains the increased errors observed in these cases.

The global nature of Chebyshev, Jacobi, and Fourier basis functions displayed a notable deterioration in performance when transitioning from architecture A1 to A2. This deterioration was particularly pronounced in the Helmholtz, Wave, and Cavity cases, where errors increased dramatically or even exceeded 90%, suggesting instability of training or an inability to generalize effectively. The global influence of these basis functions causes their values to affect the entire domain, leading to pronounced oscillations when the number of learnable parameters is increased. This issue becomes more critical in high-dimensional problems or problems with complex boundary conditions, where localized adjustments are necessary for accurate solution representation. In particular, the Fourier basis tends to suffer from the Gibbs phenomenon in scenarios involving sharp boundaries or non-periodic behavior, leading to significant oscillatory errors.

Future works. The combination of KANs and MLPs holds promise for achieving both interpretability and expressiveness in neural PDE solvers. While MLPs are well-suited for capturing broad system behaviors due to their simpler architecture and effective global fitting capability, KANs excel in capturing localized phenomena with greater precision. An interesting future work would be leveraging the efficiency of MLPs for global pattern recognition during initial solution phases, followed by the utilization of KANs with B-spline basis functions for fine-grained local refinement. This approach may balance computational efficiency and precision, similar to hybrid optimization methods such as combining gradient descent with Adam for initial training and L-BFGS strategies for further refinement. However, given the architectural differences, a significant challenge remains in the effectively transferring weights from MLPs to KANs. Addressing this requires investigating transfer learning methods such as parameter freezing, layer-wise adaptation, and model blending techniques, aiming to smoothly transition from global exploration to local refinement phases during training. Techniques like curriculum learning could also support this process by providing a structured learning schedule that progressively refines model accuracy as training progresses.

Another area for future work is investigating each model's generalization and overfitting challenges. Both architectures require further study to understand the nuances of their generalization capabilities.

Additionally, utilizing Neural Architecture Search (NAS) techniques will allow to identify optimal network architectures tailored to specific PDE types, enhancing both training efficiency and accuracy [58]. Recent studies on NAS-guided PINNs have demonstrated that shallow networks with a higher density of neurons can outperform deeper architectures for certain PDEs, particularly in achieving faster convergence and reduced computational overhead. Therefore, future work could incorporate bi-level optimization frameworks to dynamically adapt network depth and neuron distribution, as suggested by the latest advances in NAS-PINNs.

7. Conclusion

In this work, we have explored the application of different neural network architectures, MLPs and KANs, for solving various types of PDEs. Our comparative analysis focused on activation functions or basis functions to determine how these choices impact model performance across a range of PDE types. We found that while MLPs exhibit strong capabilities for broad, global function approximation due to their simpler architectures, KANs offer greater precision in modeling localized features, particularly when equipped with basis functions like B-splines. The results show that for simpler problems, such as Helmholtz and Klein-Gordon equations, increasing the number of network parameters can lead to training instability, which impacts testing performance. Conversely, KANs exhibit enhanced performance for complex problems that require fine-grained control, such as the Cavity problem. Activation functions have a significant impact on model performance. In particular, the Tanh activation function demonstrated higher accuracy for wave-like PDEs, likely due to the smooth global features characteristic of these problems, which align well with the spectral bias and smoothness characteristics of MLP with Tanh activation function. While the parametric Tanh function offers additional flexibility, it displayed inconsistent performance under certain conditions. B-splines and GRBFs are particularly effective for capturing localized features such as PDEs with local sharp gradients. B-spline basis functions consistently exhibit smoother optimization with reduced spectral bias, whereas Tanh and parametric-Tanh activations show delayed stabilization, indicating a preference for learning low-frequency components. In contrast, globally supported basis functions such as Fourier, Chebyshev, and Jacobi struggled in scenarios involving sharp transitions, often suffering from oscillatory errors.

Instabilities in the Hessian, particularly for the physics loss term, highlight the need for advanced optimization techniques to manage the highly nonconvex problem of PINN loss function and the complex high-frequency nature of these domains. A key insight from this study is that the combination of MLPs and KANs can be strategically leveraged to achieve both computational efficiency and accuracy in solving PDEs. Using MLPs for initial, global

pattern recognition and refining the solution with KANs could provide a balanced approach to managing computational resources while maintaining precision. However, challenges such as the effective transfer of weights between these architectures still need to be addressed.

Overall, this work contributes to a better understanding of how architectural and activation function choices affect the capabilities of neural networks in solving PDEs. The findings provide a foundation for developing more robust, accurate, and efficient neural PDE solvers to bridge the gap between traditional numerical methods and emerging machine-learning approaches.

Acknowledgment

We thank the National Center for High-Performance Computing of Turkey (UHeM) for providing computing resources under grant number 5010662021.

CRedit authorship contribution statement

Afrah Farea: Writing – review & editing, Writing – original draft, Visualization, Validation, Software, Methodology, Investigation, Formal analysis, Data curation, Conceptualization. **Mustafa Serdar Celebi:** Writing – review & editing, Supervision, Funding acquisition.

References

- [1] Anagnostopoulos, S.J., Toscano, J.D., Stergiopoulos, N., Karniadakis, G.E., 2024. Residual-based attention in physics-informed neural networks. *Computer Methods in Applied Mechanics and Engineering* 421, 116805.
- [2] Apicella, A., Donnarumma, F., Isgrò, F., Prevete, R., 2021. A survey on modern trainable activation functions. *Neural Networks* 138, 14–32.
- [3] Arzani, A., Wang, J.X., D’Souza, R.M., 2021. Uncovering near-wall blood flow from sparse data with physics-informed neural networks. *Physics of Fluids* 33, 071905.
- [4] Badia, S., Li, W., Martín, A.F., 2024. Finite element interpolated neural networks for solving forward and inverse problems. *Computer Methods in Applied Mechanics and Engineering* 418, 116505.
- [5] Bai, J., Liu, G.R., Gupta, A., Alzubaidi, L., Feng, X.Q., Gu, Y., 2023. Physics-informed radial basis network (pirbn): A local approximating neural network for solving nonlinear partial differential equations. *Computer Methods in Applied Mechanics and Engineering* 415, 116290.
- [6] Bischof, R., Kraus, M., 2021. Multi-objective loss balancing for physics-informed deep learning. *arXiv preprint arXiv:2110.09813*.
- [7] Bozorgasl, Z., Chen, H., 2024. Wav-kan: Wavelet kolmogorov-arnold networks. *arXiv preprint arXiv:2405.12832*.
- [8] Briggs, W.L., Henson, V.E., McCormick, S.F., 2000. *A multigrid tutorial*. SIAM.
- [9] Cai, W., Xu, Z.Q.J., 2019. Multi-scale deep neural networks for solving high dimensional pdes. *arXiv preprint arXiv:1910.11710*.
- [10] Cuomo, S., Di Cola, V.S., Giampaolo, F., Rozza, G., Raissi, M., Piccialli, F., 2022. Scientific machine learning through physics-informed neural networks: Where we are and what’s next. *Journal of Scientific Computing* 92, 88.
- [11] Cybenko, G., 1989. Approximation by superpositions of a sigmoidal function. *Mathematics of Control, Signals and Systems* 2, 303–314.
- [12] De Boor, C., 1972. On calculating with b-splines. *Journal of Approximation theory* 6, 50–62.
- [13] Dolean, V., Heinlein, A., Mishra, S., Moseley, B., 2024. Multilevel domain decomposition-based architectures for physics-informed neural networks. *Computer Methods in Applied Mechanics and Engineering* 429, 117116.
- [14] Ghorbani, B., Krishnan, S., Xiao, Y., 2019. An investigation into neural net optimization via hessian eigenvalue density, in: *International Conference on Machine Learning*, PMLR. pp. 2232–2241.
- [15] Hong, Q., Siegel, J.W., Tan, Q., Xu, J., 2022. On the activation function dependence of the spectral bias of neural networks. *arXiv preprint arXiv:2208.04924*.
- [16] Huang, X., Alkhalifah, T., 2024. Efficient physics-informed neural networks using hash encoding. *Journal of Computational Physics* 501, 112760.
- [17] Jagtap, A.D., Kawaguchi, K., Karniadakis, G.E., 2020. Adaptive activation functions accelerate convergence in deep and physics-informed neural networks. *Journal of Computational Physics* 404, 109136.
- [18] Jin, X., Cai, S., Li, H., Karniadakis, G.E., 2021. Nsfnets (navier-stokes flow nets): Physics-informed neural networks for the incompressible navier-stokes equations. *Journal of Computational Physics* 426, 109951.
- [19] Karniadakis, G.E., Kevrekidis, I.G., Lu, L., Perdikaris, P., Wang, S., Yang, L., 2021. Physics-informed machine learning. *Nature Reviews Physics* 3, 422–440.
- [20] Koenig, B.C., Kim, S., Deng, S., 2024. KAN-ODEs: Kolmogorov–Arnold network ordinary differential equations for learning dynamical systems and hidden physics. *Computer Methods in Applied Mechanics and Engineering* 432, 117397.
- [21] Kolmogorov, A.N., 1957. On the representation of continuous functions of many variables by superposition of continuous functions of one variable and addition. *Doklady Akademii Nauk SSSR* 114, 953–956.
- [22] Lagaris, I.E., Likas, A., Fotiadis, D.I., 1998. Artificial neural networks for solving ordinary and partial differential equations. *IEEE transactions on neural networks* 9, 987–1000.
- [23] Li, Z., 2024. Kolmogorov-arnold networks are radial basis function networks. *arXiv preprint arXiv:2405.06721*.
- [24] Liu, Y., Liu, W., Yan, X., Guo, S., Zhang, C.a., 2023. Adaptive transfer learning for pinn. *Journal of Computational Physics* 490, 112291.

- [25] Liu, Y., Wu, R., Jiang, Y., . Binary structured physics-informed neural networks for solving equations with rapidly changing solutions 518, 113341. URL: <https://linkinghub.elsevier.com/retrieve/pii/S0021999124005898>, doi:10.1016/j.jcp.2024.113341.
- [26] Liu, Z., Wang, Y., Vaidya, S., Ruehle, F., Halverson, J., Soljačić, M., Hou, T.Y., Tegmark, M., 2024. Kolmogorov-arnold networks. arXiv preprint arXiv:2404.19756 .
- [27] McClenny, L., Braga-Neto, U., 2020. Self-adaptive physics-informed neural networks using a soft attention mechanism. arXiv preprint arXiv:2009.04544 .
- [28] McClenny, L.D., Braga-Neto, U.M., 2023. Self-adaptive physics-informed neural networks. *Journal of Computational Physics* 474, 111722.
- [29] Mendez, M.A., Ianiro, A., Noack, B.R., Brunton, S.L., 2023. Data-driven fluid mechanics: combining first principles and machine learning. Cambridge University Press.
- [30] Montavon, G., Müller, K.R., . Neural networks-tricks of the trade second edition .
- [31] Moseley, B., Markham, A., Nissen-Meyer, T., 2023. Finite basis physics-informed neural networks (fbpinns): a scalable domain decomposition approach for solving differential equations. *Advances in Computational Mathematics* 49, 62.
- [32] Mostajeran, F., Mokhtari, R., 2022. Deepbhcp: Deep neural network algorithm for solving backward heat conduction problems. *Computer Physics Communications* 272, 108236. doi:<https://doi.org/10.1016/j.cpc.2021.108236>.
- [33] Patra, S., Panda, S., Parida, B.K., Arya, M., Jacobs, K., Bondar, D.I., Sen, A., 2024. Physics informed kolmogorov-arnold neural networks for dynamical analysis via efficient-kan and wav-kan. arXiv:2407.18373.
- [34] Rahaman, N., Baratin, A., Arpit, D., Draxler, F., Lin, M., Hamprecht, F., Bengio, Y., Courville, A., 2019. On the spectral bias of neural networks, in: *International conference on machine learning*, PMLR. pp. 5301–5310.
- [35] Raissi, M., Perdikaris, P., Karniadakis, G.E., 2019. Physics-informed neural networks: A deep learning framework for solving forward and inverse problems involving nonlinear partial differential equations. *Journal of Computational Physics* 378, 686–707.
- [36] Ramachandran, P., Zoph, B., Le, Q.V., 2017. Searching for activation functions. arXiv preprint arXiv:1710.05941 .
- [37] Rathore, P., Lei, W., Frangella, Z., Lu, L., Udell, M., 2024. Challenges in training pinns: A loss landscape perspective. arXiv preprint arXiv:2402.01868 .
- [38] Rezaei, S., Harandi, A., Moeineddin, A., Xu, B.X., Reese, S., 2022. A mixed formulation for physics-informed neural networks as a potential solver for engineering problems in heterogeneous domains: Comparison with finite element method. *Computer Methods in Applied Mechanics and Engineering* 401, 115616.
- [39] Rigas, S., Papachristou, M., Papadopoulos, T., Anagnostopoulos, F., Alexandridis, G., 2024. Adaptive training of grid-dependent physics-informed kolmogorov-arnold networks. arXiv preprint arXiv:2407.17611 .
- [40] Roy, P., Castonguay, S.T., 2024. Exact enforcement of temporal continuity in sequential physics-informed neural networks. *Computer Methods in Applied Mechanics and Engineering* 430, 117197.
- [41] Seydi, S.T., 2024. Unveiling the power of wavelets: A wavelet-based kolmogorov-arnold network for hyperspectral image classification. arXiv preprint arXiv:2406.07869 .
- [42] Shukla, K., Toscano, J.D., Wang, Z., Zou, Z., Karniadakis, G.E., 2024. A comprehensive and fair comparison between mlp and kan representations for differential equations and operator networks. *Journal of Computational Physics* 42, 789–812.
- [43] Song, Y., Wang, H., Yang, H., Taccari, M.L., Chen, X., 2024. Loss-attentional physics-informed neural networks. *Journal of Computational Physics* 501, 112781.
- [44] SS, S., 2024. Chebyshev polynomial-based kolmogorov-arnold networks: An efficient architecture for nonlinear function approximation. arXiv preprint arXiv:2405.07200 .
- [45] Sütthof, L.R., Brieger, F., Finger, H., Füllhase, S., Pipa, G., 2020. Adaptive blending units: Trainable activation functions for deep neural networks, in: *Intelligent Computing: Proceedings of the 2020 Computing Conference, Volume 3*, Springer. pp. 37–50.
- [46] Ta, H.T., 2024. Bsrbf-kan: A combination of b-splines and radial basic functions in kolmogorov-arnold networks. arXiv preprint arXiv:2406.11173 .
- [47] Takamoto, M., Praditia, T., Leiteritz, R., MacKinlay, D., Alesiani, F., Pflüger, D., Niepert, M., 2022. Pdebench: An extensive benchmark for scientific machine learning. *Advances in Neural Information Processing Systems* 35, 1596–1611.
- [48] Tancik, M., Srinivasan, P., Mildenhall, B., Fridovich-Keil, S., Raghavan, N., Singhal, U., Ramamoorthi, R., Barron, J., Ng, R., 2020. Fourier features let networks learn high frequency functions in low dimensional domains. *Advances in neural information processing systems* 33, 7537–7547.
- [49] Tang, K., Wan, X., Yang, C., 2023. Das-pinns: A deep adaptive sampling method for solving high-dimensional partial differential equations. *Journal of Computational Physics* 476, 111868.
- [50] Trottenberg, U., Oosterlee, C.W., Schuller, A., 2000. *Multigrid*. Elsevier.
- [51] Wang, H., Lu, L., Song, S., Huang, G., 2023. Learning specialized activation functions for physics-informed neural networks. arXiv preprint arXiv:2308.04073 .
- [52] Wang, J., Feng, X., Xu, H., 2024a. Adaptive sampling points based multi-scale residual network for solving partial differential equations. *Computers & Mathematics with Applications* 169, 223–236.
- [53] Wang, S., Teng, Y., Perdikaris, P., 2021. Understanding and Mitigating Gradient Flow Pathologies in Physics-Informed Neural Networks. *SIAM Journal on Scientific Computing* 43, A3055–A3081. doi:10.1137/20M1318043.
- [54] Wang, S., Yu, X., Perdikaris, P., 2022. When and why pinns fail to train: A neural tangent kernel perspective. *Journal of Computational Physics* 449, 110768.
- [55] Wang, Y., Siegel, J.W., Liu, Z., Hou, T.Y., 2024b. On the expressiveness and spectral bias of kans. arXiv preprint arXiv:2410.01803 .
- [56] Wang, Y., Sun, J., Bai, J., Anitescu, C., Eshaghi, M.S., Zhuang, X., Rabczuk, T., Liu, Y., 2024c. Kolmogorov arnold informed neural network: A physics-informed deep learning framework for solving pdes based on kolmogorov arnold networks. arXiv preprint arXiv:2406.11045 .
- [57] Wang, Y., Yao, Y., Guo, J., Gao, Z., 2024d. A practical pinn framework for multi-scale problems with multi-magnitude loss terms. *Journal of Computational Physics* 510, 113112.

- [58] Wang, Y., Zhong, L., 2024. NAS-PINN: Neural architecture search-guided physics-informed neural network for solving PDEs. *Journal of Computational Physics* 496, 112603. doi:10.1016/j.jcp.2023.112603.
- [59] Wu, C., Zhu, M., Tan, Q., Kartha, Y., Lu, L., 2023. A comprehensive study of non-adaptive and residual-based adaptive sampling for physics-informed neural networks. *Computer Methods in Applied Mechanics and Engineering* 403, 115671.
- [60] Xu, J., Chen, Z., Li, J., Yang, S., Wang, W., Hu, X., Ngai, E.C.H., 2024. Fourierkan-gcf: Fourier kolmogorov-arnold network—an effective and efficient feature transformation for graph collaborative filtering. *arXiv preprint arXiv:2406.01034* .
- [61] Xu, Z.Q.J., 2020. Frequency principle: Fourier analysis sheds light on deep neural networks. *Communications in Computational Physics* 28, 1746–1767.
- [62] Yang, S., Kim, H., Hong, Y., Yee, K., Maulik, R., Kang, N., 2024. Data-driven physics-informed neural networks: A digital twin perspective. *Computer Methods in Applied Mechanics and Engineering* 428, 117075.
- [63] Yao, Z., Gholami, A., Keutzer, K., Mahoney, M.W., 2020. Pyhessian: Neural networks through the lens of the hessian, in: 2020 IEEE international conference on big data (Big data), IEEE. pp. 581–590.
- [64] Zeng, C., Wang, J., Shen, H., Wang, Q., 2024. Kan versus mlp on irregular or noisy functions. *arXiv preprint arXiv:2408.07906* .
- [65] Zhang, D., Li, Y., Ying, S., 2024. Trans-net: A transferable pretrained neural networks based on temporal domain decomposition for solving partial differential equations. *Computer Physics Communications* 299, 109130. doi:<https://doi.org/10.1016/j.cpc.2024.109130>.
- [66] Zhang, J., Ding, C., 2024. Simple yet effective adaptive activation functions for physics-informed neural networks. *Computer Physics Communications* , 109428doi:<https://doi.org/10.1016/j.cpc.2024.109428>.
- [67] Zhao, H., Hao, Y., Xu, W., Li, C., 2024. Adaptive-sampling physics-informed neural network for viscoacoustic wavefield simulation. *IEEE Geoscience and Remote Sensing Letters* .